JACS
JOURNAL OF THE AMERICAN CHEMICAL SOCIETY

ARTICLE

pubs.acs.org/JACS

Simultaneous Bridge-Localized and Mixed-Valence Character in Diruthenium Radical Cations Featuring Diethynylaromatic Bridging Ligands

Mark A. Fox,[†] Boris Le Guennic,[‡,§] Rachel L. Roberts,[†] Daniel A. Brue,[†] Dmitry S. Yufit,[†] Judith A. K. Howard,[†] Gabriele Manca,[‡,⊥] Jean-François Halet,[‡] František Hartl,[∥] and Paul J. Low*[,†]

[†]Department of Chemistry, Durham University, South Road, Durham DH1 3LE, U.K.

[‡]Laboratoire des Sciences Chimiques de Rennes, UMR 6226 CNRS-Université de Rennes 1, 35042 Rennes cedex, France

[§]Université de Lyon, CNRS, Institut de Chimie de Lyon, Ecole Normale Supérieure de Lyon, 15 parvis René Descartes, BP7000, 69342 Lyon Cedex 07, France

[⊥]Istituto di Chimica dei Composti Organometallici, ICCOM-CNR, Via Madonna del Piano 10, 50019 Sesto Fiorentino, Florence, Italy

[∥]Department of Chemistry, University of Reading, Whiteknights, Reading RG6 6AD, U.K.

Supporting Information

ABSTRACT: A series of bimetallic ruthenium complexes [{Ru(dppe)Cp*}$_2$(μ-C≡CArC≡C)] featuring diethynylaromatic bridging ligands (Ar = 1,4-phenylene, 1,4-naphthylene, 9,10-anthrylene) have been prepared and some representative molecular structures determined. A combination of UV−vis−NIR and IR spectroelectrochemical methods and density functional theory (DFT) have been used to demonstrate that one-electron oxidation of compounds [{Ru(dppe)Cp*}$_2$(μ-C≡CArC≡C)](HC≡CArC≡CH = 1,4-diethynylbenzene; 1,4-diethynyl-2,5-dimethoxybenzene; 1,4-diethynylnaphthalene; 9,10-diethynylanthracene) yields solutions containing radical cations that exhibit characteristics of both oxidation of the diethynylaromatic portion of the bridge, and a mixed-valence state. The simultaneous population of bridge-oxidized and mixed-valence states is likely related to a number of factors, including orientation of the plane of the aromatic portion of the bridging ligand with respect to the metal d-orbitals of appropriate π-symmetry.

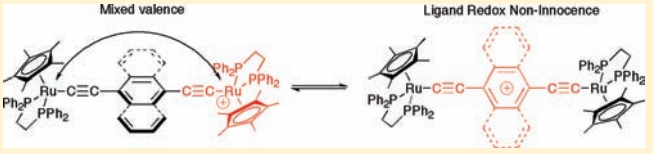

INTRODUCTION

Open-shell bimetallic complexes [{ML$_n$}(μ-bridge){ML$_n$}]$^{n\pm}$, in which two metal centers or clusters, M, supported by auxiliary ligands, L, are linked via some conjugated bridging ligand, continue to attract unabated attention that is driven by a desire (1) to better understand the nature of the factors affecting charge localization in solution[1] and solid state[2,3] and the thermal and photoinduced intramolecular electron transfer events that can occur between the various components of these molecular systems[4−8] and (2) to identify systems suitable for use in the development of molecular-scale wires and other components for molecular electronics.[9−17] In the case of complexes within which the unpaired electron or hole is localized on one of the metal centers, M, the systems may be described in terms of the classical, two-state concepts of mixed valency.[4,18−23] For example, in [{Fe(dppe)Cp*}$_2$-(μ-C≡CC$_6$H$_4$C≡C)] (**1a**) the Fe(dppe)Cp* fragment offers a pair of almost degenerate d-type orbitals of appropriate symmetry to interact with the ethynyl π-orbitals of the bridging ligand fragment, but typically lying somewhat higher in energy. Consequently, the frontier orbitals of ethynyl derivatives of this metal auxiliary are highly metallic in character, and the redox chemistry of these complexes is often satisfactorily described in terms of Fe(II/III) couples.[24] In the case of bimetallic iron complexes shown in Chart 1, broadly speaking, [**1a**]$^+$ is an example of a strongly coupled mixed-valence complex on the borderline between Classes II and III.[25−27] Although the cation [**1b**]$^+$ behaves in a manner similar to that of [**1a**]$^+$,[28] extension of the aromatic bridging unit in [**1c**]$^+$ leads to significantly more bridge character in the SOMO, giving rise to a more delocalized system.[29] Given the substantive electron spin density calculated on the diethynyl anthracene moiety in [**1c**]$^+$ (68%) and the significant carbon radical character evidenced by a combination of EPR and Mössbauer spectroscopies, the description of [**1c**]$^+$ in terms of a redox noninnocent bridging ligand may also be appropriate. In contrast, insertion of an additional phenylene spacer, as in [**1d**]$^+$, results in a system that is better classified in terms of a weakly coupled (Class II) mixed-valence system.[30]

Interestingly, the Mössbauer spectrum of polycrystalline samples of [**1a**]$^+$ is consistent with a solid solution containing both the mixed-valence (valence trapped) form, and a 'detrapped' component, the proportions of which are found to vary from sample to sample with recrystallization. This behavior has been attributed to variations in local environment brought about by

Received: August 18, 2011
Published: September 29, 2011

Chart 1. Complexes 1a−d

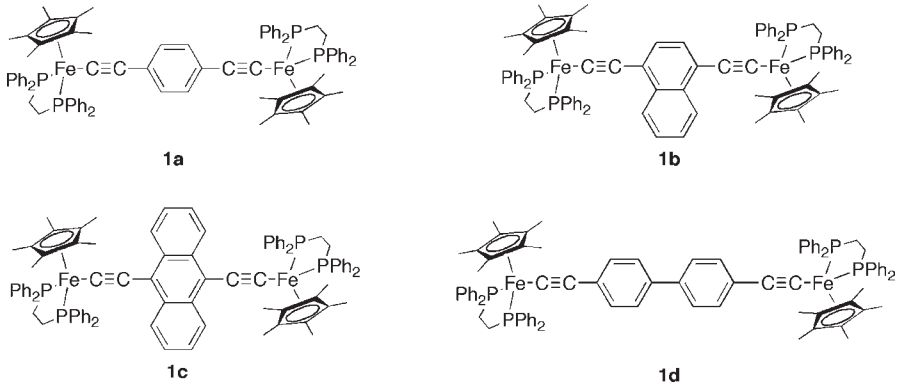

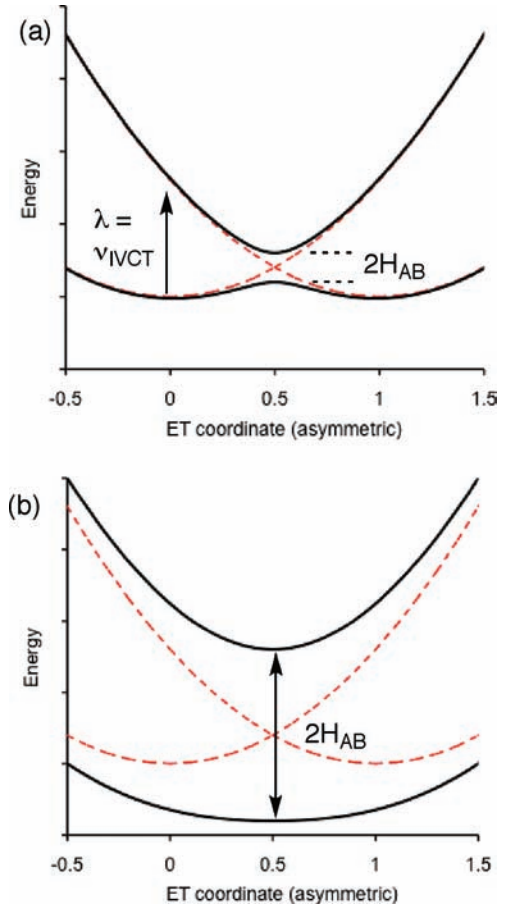

Figure 1. Diabatic (broken line) and adiabatic (solid line) potential energy surfaces for (a) a weakly coupled (Robin and Day Class II) symmetric mixed-valence complex and (b) a strongly coupled (Robin and Day Class III) symmetric mixed-valence complex.

differences in crystal forms, or delocalization of the odd electron into a π-orbital on the bridging ligand.[25] Such observations serve as a prelude to more detailed and ongoing discussions of the role the relative conformation of the bridging ligand with respect to the metal centers plays in determining the magnitude of electronic coupling between metal centers,[31−38] and the role of bridge conformation not only in switching between mixed-valence classes but also in controlling the metal vs bridging-ligand character of the redox processes in $[\{ML_n\}(\mu\text{-bridge})\{ML_n\}]$ systems.[39,40]

Examples of systems related to $[\mathbf{1c}]^+$ in which the unpaired electron/hole is delocalized over both metals and the bridging ligand, and hence not well described by a simple two-state mixed-valence model, or even localized on the bridging or support ligands, are becoming more widely recognized and demand alternative descriptions.[18,35,41−54] For example, the general notion of 'redox noninnocent' bridging ligands in $[\{ML_n\}(\mu\text{-bridge})\{ML_n\}]^{n\pm}$ systems is well documented,[55,56] and treatments of the potential energy surfaces associated with $[\{ML_n\}(\mu\text{-bridge})\{ML_n\}]^{n\pm}$ systems (and analogous compounds based on organic rather than metal-based electrophores) in terms of three-center models have long been known[57−61] and continue to be refined.[18,38,62−67] The details of the various models have been discussed thoroughly in these latter papers, and a short review of these variata has been presented by Launay;[62] thus, only the features of the evolution from the two- to three-state model relevant to the present discussion are described here.

In the two-state description of a symmetric mixed-valence system developed by Marcus, Hush, and others two diabatic potential energy curves are constructed (usually taken as parabola from a harmonic approximation), representing the energetically degenerate states $[\{M_AL_n\}^+(\mu\text{-bridge})\{M_BL_n\}]$ and $[\{M_AL_n\}(\mu\text{-bridge})\{M_BL_n\}^+]$ (the A and B subscripts being used for convenience to distinguish the metal sites). By permitting a small degree of electronic coupling H_{AB} between these two adiabatic states, the familiar double-potential well diagram is obtained (Figure 1a), the minima usually being placed at 0 and 1 (or $\pm 1/2$) on the electron transfer coordinate axis and the system being referred to as belonging to Class II in the Robin and Day classification scheme. The thermal barrier that lies at the midpoint to the minima on the ground-state curve arises from the different equilibrium M−L and M−bridge bond lengths and solvent configurations at the donor ($\{ML_n\}$) and acceptor ($\{ML_n\}^+$) sites associated with the differences in metal oxidation state. At this intermediate point the inner- and outer-sphere geometries at the metal centers are identical, and electron transfer can take place without further input of energy to the system. The progression from one minimum to the other constitutes the electron transfer reaction, e.g. $[\{M_AL_n\}^+(\mu\text{-bridge})\{M_BL_n\}] \rightarrow [\{M_AL_n\}(\mu\text{-bridge})\{M_BL_n\}^+]$.

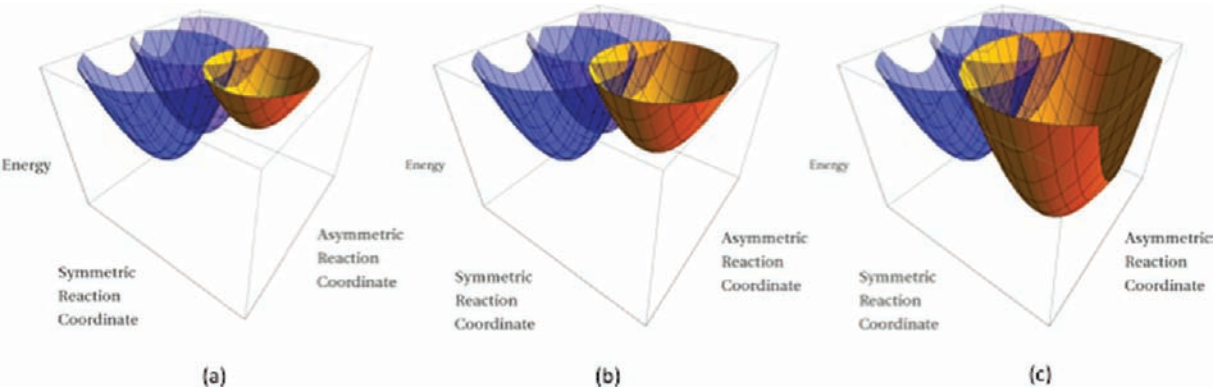

Figure 2. Sketches of the diabatic potential energy surfaces associated with the three-state description of a $[\{ML_n\}(\mu\text{-bridge})\{ML_n\}]^+$ system for arbitrary displacement of the bridge state (yellow) along the symmetric reaction coordinate d from the mixed-valence states (blue): (a) The bridge state lies high in energy above the mixed-valence states, $\Delta \gg 0$; (b) the bridge state is low lying in energy and provides a pathway for electron-hopping between the metallic states $\Delta > 0$; (c) the bridge state is lower in energy than the mixed-valence states ($\Delta < 0$), and the system is better described in terms of a redox noninnocent bridging ligand with the charge residing on the bridge.

The overall change in the geometry of the system corresponds to an asymmetric stretch of the system, and the reaction coordinate is often described in these terms.[57] The vertical transition from the ground-state minima to the higher-lying (excited) state gives rise to the well-known intervalence charge transfer (IVCT) transition and, in a weakly coupled system, corresponds to the reorganization energy necessary to move an electron from the donor site to the acceptor site. As coupling between the diabatic states increases, the thermal barrier to electron transfer decreases, and in the strong coupling limit (Robin and Day Class III) the lower potential energy takes on a single minimum, and the optical absorption loses charge transfer character and becomes better described in terms of a transition between molecular orbitals that are delocalized over the molecule (Figure 1).

If in addition to the metal centers, the bridging-ligand B also offers a low-lying (redox) state, it is necessary to augment the elementary two-state description by introduction of a third state that explicitly allows for the population of the bridge, $[\{ML_n\}(\mu\text{-bridge})^+\{ML_n\}]$. The coupling of this third state to the two states describing the localization of charge at the metal centers leads to deviations in the shape of the resulting adiabatic free-energy curves from the predictions of the two-state model, the most obvious being the presence of a third minimum along the asymmetric coordinate midway between the 'reactant' and 'product' states of the electron transfer reaction. If this additional state is sufficiently low lying to be populated, then an electron-hopping model for electron transfer becomes possible.[63] Further consequences of the presence of a low-lying bridge state have been discussed in detail by Brunschwig, Creutz, and Sutin and include a narrowing and increase in intensity of the IVCT transition as the magnitude of the coupling between the three diabatic states increases,[18] and the presence of an MLCT/LMCT band the shape and energy of which are also intimately related to the coupling of the three states.[38] In contrast, in the limit of weak coupling, the three-state solution parallels that of the two-state model.[18]

If the bridge is treated as a singular component, transfer of charge to (or from) the bridge affects the associated bonds in a symmetrical manner. To account for this symmetric mode, it is necessary to extend the description of the potential energy curves to include a second (symmetric) reaction coordinate axis and to consider the three-dimensional (3-D) potential energy surfaces. The traditional Marcus−Hush curves are simply slices through these 3-D (asymmetric, symmetric, and energy) surfaces at a fixed point along the symmetric coordinate. The diabatic description of the three-state system $[\{M_AL_n\}(\mu\text{-bridge})\{M_BL_n\}]^+$ now involves three paraboloids, representing localization of charge at M_AL_n, bridge, and M_BL_n (Figure 2), the general disposition of which can be defined in terms of the relative energy of the minima (taken as 0, Δ, and 0 in the case $M_AL_n = M_BL_n$), and the displacement of the bridge minimum along the symmetric reaction coordinate relative to the minima that represent localization of charge on the metal centers, d. Together, Δ and d define the position of the bridge state with respect to the double potentials that describe the mixed-valence state.[62] Allowing these three states to couple generates a 3-D adiabatic surface; the number, depth, and definition of minima are dependent on the magnitude of the individual couplings between the diabatic states H_{ij}, Δ, and d. For the systems in which Δ is positive (i.e., the bridge state lies at higher energy than the mixed-valence state) the bridge state leads to either a bay or third minimum above the double minimum of the mixed-valence state. The presence of the additional minimum has been shown to permit both superexchange and hopping mechanisms to operate in suitably designed systems based on redox-active triaryl amines linked by a relatively electron-rich 1,4-diethynyl-2,5-dimethoxybenzene bridge.[63] For systems with increasingly negative Δ, the ground-state potential energy surface evolves toward a single minimum, and the system can be treated as a bridge-based electrophore with pendent metal groups. In such cases the low energy transitions in metal based $[\{ML_n\}(\mu\text{-bridge})^+\{ML_n\}]$ systems have considerable MLCT character.[64]

Against this backdrop of possible classes of electronic structure associated with $[\{ML_n\}(\mu\text{-bridge})\{ML_n\}]^{n\pm}$ systems, complexes based on Ru(dppe)Cp* and other electron-rich Ru(II) fragments offer an interesting counterpoint. The metal orbitals of the exemplary Ru(dppe)Cp* fragment lie significantly lower in energy than the Fe-based orbitals in the analogous Fe(dppe)Cp* fragment. As a result, the metal character in the frontier orbitals of Ru-based alkynyl and vinyl complexes is greatly reduced, and the unsaturated hydrocarbon ligand is often found to contribute substantially to the frontier orbitals of these systems in various oxidation states; i.e., the ruthenium complexes exhibit ligand redox noninnocent character.[68,69] Given the redox noninnocent

Chart 2. The complexes 2−5 involved in this study[87]

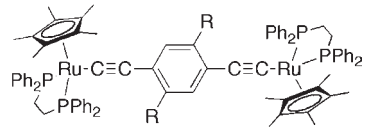

R = H (**2**), OMe (**3**)

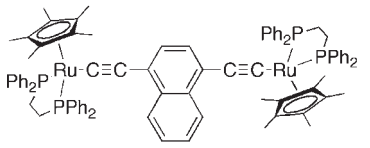

4

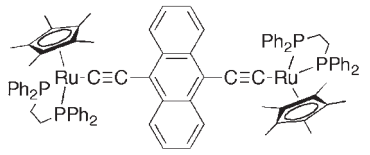

5

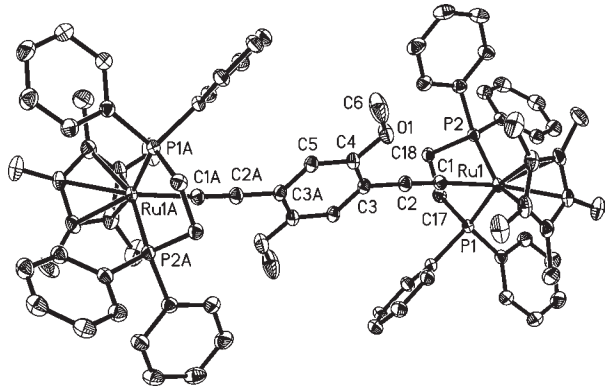

Figure 3. Molecular structure of **3** showing the atom labeling scheme. Hydrogen atoms have been removed for clarity. Displacement ellipsoids are plotted at 50%.

behavior of the arylethynyl ligand in monometallic $[Ru(C{\equiv}CArX)(dppe)Cp^*]^+$ complexes, a re-examination of the nature (mixed valence or otherwise) of the radical cations that are derived from one-electron oxidation of related homo- and heterometallic ruthenium-containing complexes featuring diethynylaromatic bridging ligands is warranted.[11,51,53,70−84] In this paper we describe the synthesis of a series of bimetallic ruthenium complexes $[\{Ru(dppe)Cp^*\}_2(\mu\text{-}C{\equiv}CArC{\equiv}C)]$ featuring diethynylaromatic bridging ligands (Ar = 1,4-phenylene, 1,4-naphthylene, 9,10-anthrylene) and some representative molecular structures. Spectroscopic investigation of the monocations derived by one-electron oxidation of $[\{Ru(dppe)Cp^*\}_2(\mu\text{-}C{\equiv}CArC{\equiv}C)]$ reveals trends consistent with the population of two low-lying states: one derived from 'bridge'-based oxidation and the other with spectroscopic signatures more in keeping with a localized mixed-valence structure. The two situations probably arise through different conformations of the aromatic moiety with respect to the metal fragments, and hence there is variation

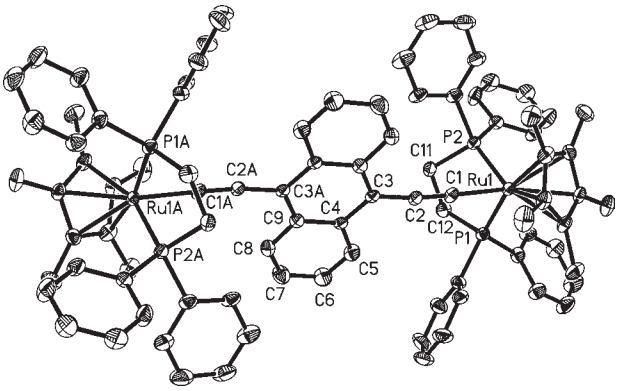

Figure 4. Molecular structure of **5** showing the atom labeling scheme. Hydrogen atoms have been removed for clarity. Displacement ellipsoids are plotted at 50%.

in the metal−bridge orbital overlaps and associated electronic couplings between components.

RESULTS AND DISCUSSION

The compounds $[\{Ru(dppe)Cp^*\}_2(\mu\text{-}C{\equiv}CArC{\equiv}C)](HC{\equiv}CArC{\equiv}CH$ = 1,4-diethynylbenzene; 1,4-diethynyl-2,5-dimethoxybenzene; 1,4-diethynylnaphthlylene; 9,10-diethynylanthracene) (**2**−**5**) (Chart 2) were prepared from $[RuCl(dppe)Cp^*]$ and the appropriate trimethylsilyl-protected dialkyne in the presence of KF.[51,78,85]

The tetrafluorobenzene derivative $[\{Ru(dppe)Cp^*\}_2(\mu\text{-}C{\equiv}C\text{-}1,4\text{-}C_6F_4{-}C{\equiv}C)]$ is the only example of a structurally characterized bimetallic ruthenium complex featuring a para-substituted diethynyl aromatic ligand of which we are aware,[51] although the structures of the iron complexes **1c**, $[\mathbf{1c}][TCNE]$ and $[\mathbf{1c}][PF_6]_2$ are known.[29] The structures of **3** (Figure 3) and **5** (Figure 4) were determined crystallographically and feature approximately linear Ru(1)−C(1)−C(2)−C(3) fragments, with the Cp* and dppe ligands and C(1) forming a pseudo-octahedral environment at each metal center (see Table 1). In each case the molecule rests on an inversion center, and as such the dihedral angle C(0)−Ru···Ru′−C(0′) (θ) is 180° [C(0) is the centroid of the Cp* ligand]. The disposition of the metal fragments with respect to the aryl fragment can be defined in terms of the C(0)−Ru(1)···C(3)−C(4) angle (ϕ) of 45.5 (**3**)/47.8 (**5**) °. The Ru−P bond lengths in **3** [2.2575(4), 2.2580(4) Å] and **5** [2.2597(17), 2.2602(16) Å] are longer than in the butadiyndiyl-bridged complex $[\{Ru(dppe)Cp^*\}_2(\mu\text{-}C{\equiv}CC{\equiv}C)]$ (2.2420(8)−2.2556(8) Å),[87] but in general the bond lengths are consistent with those of mononuclear ruthenium acetylide complexes $[Ru(C{\equiv}CArX)(dppe)Cp^*]$[69] and bimetallic $[\{Ru(dppe)Cp^*\}_2(\mu\text{-}C{\equiv}C\text{-}1,4\text{-}C_6F_4\text{-}C{\equiv}C)]$.[51] The 2,5-dimethoxy-substituted aromatic ring in **3** does not display any significant quinoidal character and is similar in structure to $HC{\equiv}CC_6H_2(OMe)_2C{\equiv}CH$,[88,89] while the bond parameters associated with the 9,10-bis(ethynyl)anthracene ligand in **5** are indistinguishable from those of the iron analogue $[\{Cp^*(dppe)Fe\}_2(\mu\text{-}C{\equiv}C\text{-}9,10\text{-}C_{14}H_8C{\equiv}C)]$.[29]

Each of the compounds **2**−**5** undergoes two sequential and reversible oxidation processes, separated by ∼300 mV in CH_2Cl_2/0.1 M NBu_4BF_4, indicating the appreciable thermodynamic stability of the compounds $[\mathbf{2}{-}\mathbf{5}]^+$ with respect to disproportionation in this solvent system, and giving rise to large

Table 1. Selected Bond Lengths (Å) and Angles (deg) from the Crystallographically Determined Structures of 3 and 5, and the DFT-Optimized Structures $[2\text{-H}]^{n+}$ and $[5\text{-H}]^{n+}$ (n = 0, 1, 2)

	3	[2-H]	$[2\text{-H}]^+$	$[2\text{-H}]^{2+}$	5	[5-H]	$[5\text{-H}]^+$	$[5\text{-H}]^{2+}$
Ru−C(1)	2.0001(15)	2.018	1.965	1.925	2.017(6)	2.016	1.971	1.931
Ru−P(1, 2)	2.2575(4), 2.2580(4)	2.277	2.302	2.320	2.260(2)	2.279	2.299	2.315
C(1)−C(2)	1.219(2)	1.228	1.242	1.257	1.228(8)	1.230	1.242	1.256
C(2)−C(3)	1.426(2)	1.423	1.393	1.368	1.416(8)	1.419	1.389	1.363
C(3)−C(4)	1.408(2)	1.413	1.429	1.447	1.422(9)	1.425	1.445	1.463
C(4)−C(5)	1.389(2)	1.388	1.375	1.362	1.428(9)	1.429	1.418	1.408
C(5)−C(6)					1.354(10)	1.371	1.379	1.388
C(6)−C(7)					1.393(10)	1.423	1.412	1.403
C(4)−C(9)					1.426(8)	1.441	1.430	1.424
P(1)−Ru−P(2)	83.86(1)	93.07	92.15	90.73	83.12(6)	93.25	92.71	91.51
Ru−C(1)−C(2)	175.0(1)	178.7	177.9	177.3	178.5(5)	179.3	177.9	177.1
C(1)−C(2)−C(3)	177.7(2)	178.5	177.8	177.3	172.8(6)	178.6	177.6	176.7
θ	180	158.9	167.0	180.0	180	180.0	179.3	175.7
ϕ	45.5	−10.3	6.2	0.0	47.8	0.0	−8.8	−2.0

Table 2. Electrochemical Data from Compounds 2−5[a]

cmpd	E_1/V	E_2/V	ΔE/mV	K_C[b]
2	0.01	0.30	290	0.8×10^5
3	−0.14	0.17	310	1.7×10^5
4	−0.06	0.24	290	0.8×10^5
5	−0.17	0.13	300	1.2×10^5

[a] CH_2Cl_2/0.1 M NBu_4BF_4, 25 °C, ν = 100 mV/s, all platinum electrodes, reported vs SCE from an internal ferrocene/ferrocenium couple (FcH/FcH^+ = 0.46 V). [b] $K_C = \exp(\Delta EF/RT)$.

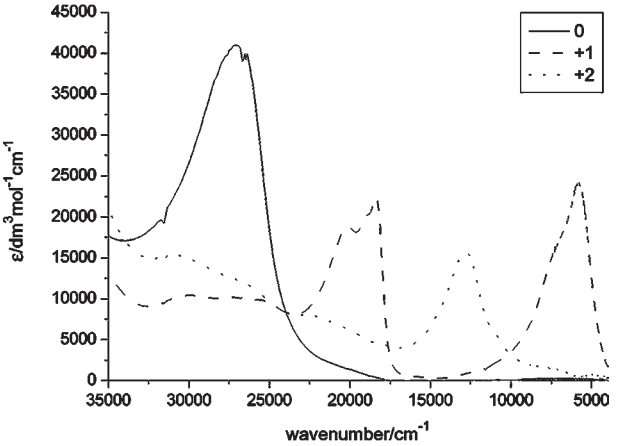

Figure 5. The UV−vis−NIR spectra of **2** (solid line), $[2]^+$ (broken line), and $[2]^{2+}$ (dotted line) collected by in situ oxidation of **2** in a spectroelectrochemical cell (CH_2Cl_2/0.1 M NBu_4BF_4), which is representative of the series $[2\text{−}5]^{n+}$.

comproportionation constants, K_C (Table 2). These oxidations become more thermodynamically favorable as a function of the size of the conjugated π-system in the aromatic bridge [e.g., $E_1(2) > E_1(4) > E_1(5)$] and through the introduction of donor groups on the bridging moiety [e.g., $E_1(2) > E_1(3)$], providing evidence for the involvement of the bridge π-system in these redox processes. In each case, a third anodic wave was also observed (**2**, 1.24 V; **3**, 1.00 V; **4**, 1.29 V; **5**, 1.29 V), but the associated trications have not been investigated further, given the complete chemical irreversibility of the last redox process.

UV−vis−NIR spectra of the compounds $[2\text{−}5]^{n+}$ were collected using spectroelectrochemical methods (CH_2Cl_2, 0.1 M NBu_4BF_4) (Figure 5). The UV−vis−NIR spectra of the neutral systems **2**−**5** are dominated by intense π−π^* bands associated with the diethynylarylene portion of these molecules, which are found somewhat lower in energy than in the trimethylsilyl-capped ligand precursors, consistent with the presence of the electron-donating metal substituents in the complexes. The largely bridging ligand-based π−π^* absorptions collapse on oxidation to $[2\text{−}5]^+$ with new, vibrationally structured aromatic radical bands growing between 19,000 (**2**)−11,000 (**5**) cm^{-1} (525−900 nm). These bands, which are very similar to those observed for aromatic radical cations,[64,90] may be taken as evidence for the redox noninnocent character of the bridging ligand,[51,53] a suggestion further supported by the results of DFT calculations (vide infra). In addition, each of $[2\text{−}5]^+$ features a relatively intense band envelope in the NIR region, which can be deconvoluted into the sum of three Gaussian-shaped sub-bands in the region of 8000−5000 cm^{-1} (1200−1800 nm). The significance of these sub-bands is discussed in more detail below. On oxidation to the dications, $[2\text{−}5]^{2+}$, these features in the visible and NIR regions collapse with a new MLCT transition (vide infra) near 14,000 cm^{-1} (700 nm), which tails into the NIR region and overlaps with a low-intensity pseudo Ru(III) dd band, observed in each case.

The involvement of the bridging ligand in the redox active orbitals in **2**−**5** evidenced by the UV−vis spectroscopy is supported by electronic structure calculations (B3LYP/3-21G*)[68] carried out on $[\{Ru(PH_3)_2Cp\}_2(\mu\text{-}C{\equiv}CC_6H_4C{\equiv}C)]^{n+}$ ($[\mathbf{2\text{-}H}]^{n+}$) and $[\{Ru(PH_3)_2Cp\}_2(\mu\text{-}C{\equiv}CC_{14}H_8C{\equiv}C)]^{n+}$ ($[\mathbf{5\text{-}H}]^{n+}$) ($n$ = 0, 1, 2), which were taken as being representative of the series **2**−**5** and related redox products. In the case of the doubly oxidized models the low-spin configuration was found to be more stable than the corresponding high-spin state (6.2 kcal.mol^{-1} $[\mathbf{2\text{-}H}]^{2+}$/20.5 kcal.$mol^{-1}$ $[\mathbf{5\text{-}H}]^{2+}$), which can be attributed to the large difference in energy between the HOMO and the other occupied orbitals (see Tables S3 and S6 in Supporting Information (SI)). The optimized

dx.doi.org/10.1021/ja207827m |J. Am. Chem. Soc. 2011, 133, 18433–18446

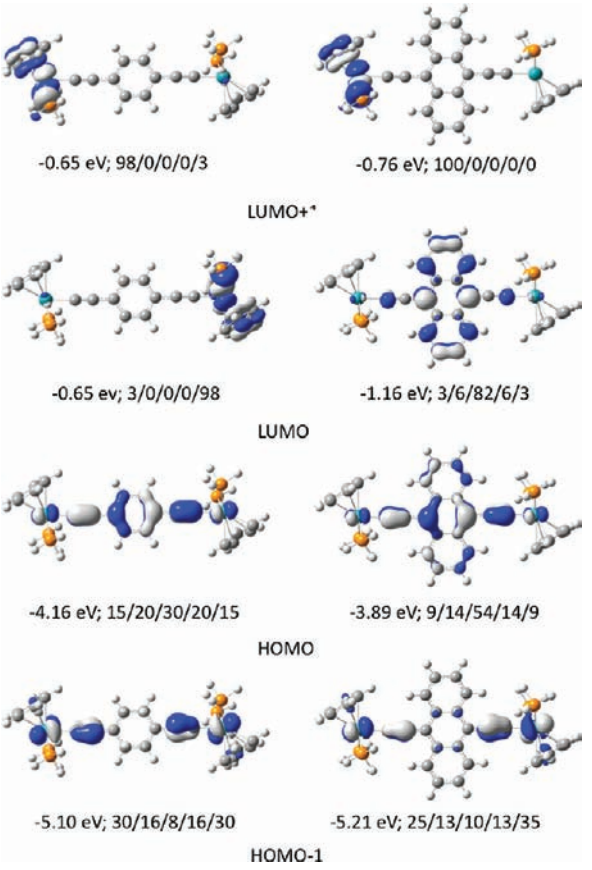

Figure 6. Selected frontier orbitals from **2-H** (left) and **5-H** (right) plotted with contour values ± 0.04 $(e/b^3)^{1/2}$. Orbital energies (eV) and composition [% $Cp(PH_3)_2Ru/C_2/Ar/C_2/Ru(PH_3)_2Cp$] are summarized numerically.

geometry of the neutral species [**2-H**] and [**5-H**] give bond lengths that are in good agreement with the crystallographically determined structures of **2** and **5**, respectively (see Table 1). The ϕ angle (defined above) in each of lowest energy structures of $[\mathbf{2\text{-}H}]^{n+}$ varies only a little, from $-10.3°$ ($n = 0$) to $6.2°$ ($n = 1$) and $0.0°$ ($n = 2$) ($[\mathbf{2\text{-}H}]^{n+}$). Minor variation in the orientation of the aromatic ring with respect to the $Ru(PH_3)_2Cp$ fragment is also noted in the structures $[\mathbf{5\text{-}H}]^{n+}$ ($n = 0$, $\phi = 0.0°$; $n = 1$, $\phi = -8.8°$; $n = 2$, $\phi = -2.0°$). Comparison of the structures of [**2-H**] and $[\mathbf{2\text{-}H}]^+$, and [**5-H**] and $[\mathbf{5\text{-}H}]^+$ reveals that the change in electron count results in modest elongation of the Ru−P bonds and contraction of the Ru−C(1) bonds. The C(1)≡C(2) bond length expands by ∼1% on oxidation, and these changes associated with the metal coordination sphere are also accompanied by the evolution of significant quinoidal character in the aromatic portion of the bridging ligand (Table 1).

Selected frontier orbitals of each of [**2-H**] and [**5-H**] are shown in Figure 6, with more complete lists of orbital energies and contributions given in the SI. In each case, the HOMO is delocalized over the metal centers and the carbon atoms of the ethynyl aromatic moieties, with considerable bridging ligand character ([**2-H**] 70%; [**5-H**] 82%). The HOMO−1 is approximately derived from the in-phase combination of the metal-d/ethynyl-π systems, and hence is more extensively localized on the metal centers and the carbon atoms of the C≡C fragment, with negligible contribution from the central aromatic fragment. The isoenergetic LUMO and LUMO+1 of [**2-H**] are associated with

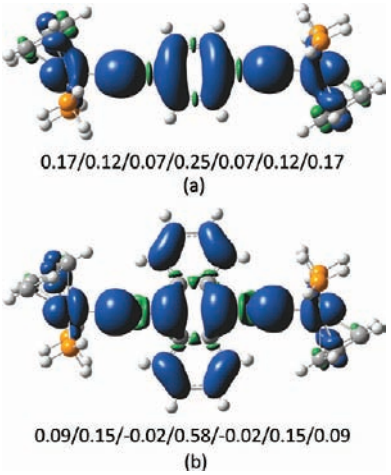

Figure 7. Plot and numerical summary (% $Ru/C_\alpha/C_\beta/Ar/C_\beta/C_\alpha/Ru$) of the spin density distribution in (a) $[\mathbf{2\text{-}H}]^+$ and (b) $[\mathbf{5\text{-}H}]^+$. Contour values: $\pm$ 0.04 e/b^3.

Chart 3. Reference Compound 6[63,64]

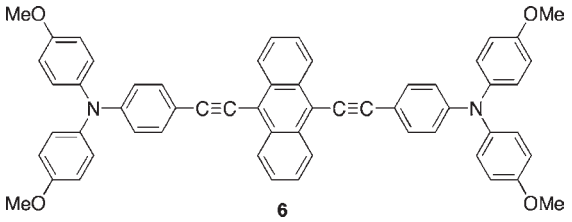

6

the $Ru(PH_3)_2Cp$ fragments, but the LUMO of the anthracene derivative [**5-H**] is predominantly anthracene π^* in character (82%), the unoccupied metal-fragment-centered orbitals being somewhat higher in energy. Although it is not possible to make quantitative comparisons of the results from [**2-H**] and [**5-H**] with calculations on related systems that have been constructed to model the iron series $[\{Fe(dppe)Cp^*\}_2(\mu\text{-}C{\equiv}CC_6H_4C{\equiv}C)]$ (**1a**)[26,29,39] and $[\{Fe(dppe)Cp^*\}_2(\mu\text{-}C{\equiv}CC_{14}H_8C{\equiv}C)]$ (**1c**) because of differences in the ligand models and computational methods employed, the frontier orbital characteristics and nodal properties of the iron and ruthenium complexes are generally similar, with a significant contribution from the anthrylene moiety to the LUMO of $[\{Fe(dHpe)Cp\}_2(\mu\text{-}C{\equiv}CC_{14}H_8C{\equiv}C)]$ (dHpe = $H_2PCH_2CH_2PH_2$) also having been calculated.[29]

The frontier orbitals of the oxidized compounds $[\mathbf{2\text{-}H}]^+$ and $[\mathbf{5\text{-}H}]^+$ are similar in composition to those of the neutral analogues, and qualitatively the oxidation process can be described in terms of the stepwise depopulation of the HOMOs of the neutral precursors. Thus, the α-highest occupied spin orbital (HOSO) and β-lowest unoccupied spin orbital (LUSO) of $[\mathbf{2\text{-}H}]^+$ and the LUMO of the (low-spin) dication $[\mathbf{2\text{-}H}]^{2+}$ are all closely related in composition to the HOMO of [**2-H**], and feature significant diethynylaromatic character. In the case of the monocations, some 64 ($[\mathbf{2\text{-}H}]^+$)−84 ($[\mathbf{5\text{-}H}]^+$) % of the calculated spin density is associated with the diethynylaromatic ligand, with the metallic contribution decreasing from 34% in $[\mathbf{2\text{-}H}]^+$ to 18% in $[\mathbf{5\text{-}H}]^+$ (Figure 7). The spin density associated with the organic bridging ligand is not distributed evenly but is associated primarily with the C_α carbon of the acetylide fragment and *ipso*-carbon atoms of

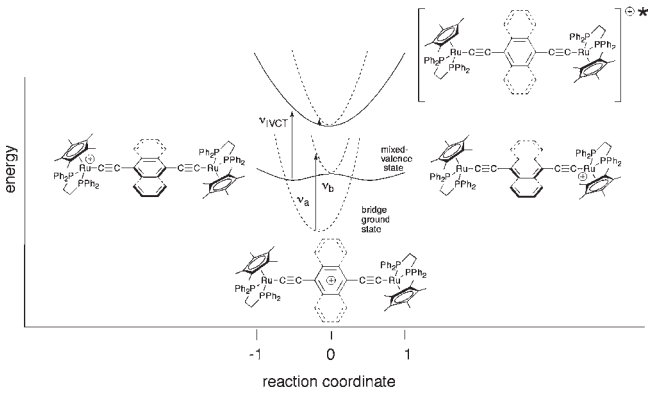

Figure 8. Schematic adiabatic potential energy curves for the bridge-based ground state in $[\mathbf{2}-\mathbf{5}]^+$. The broken curves are shown in the symmetric reaction coordinate that runs perpendicular to the asymmetric coordinate shown in the plane of the page. The minimum of the ground state may be shifted along the asymmetric coordinate relative to the relaxed conformations of the excited states. Adapted from reference 64.

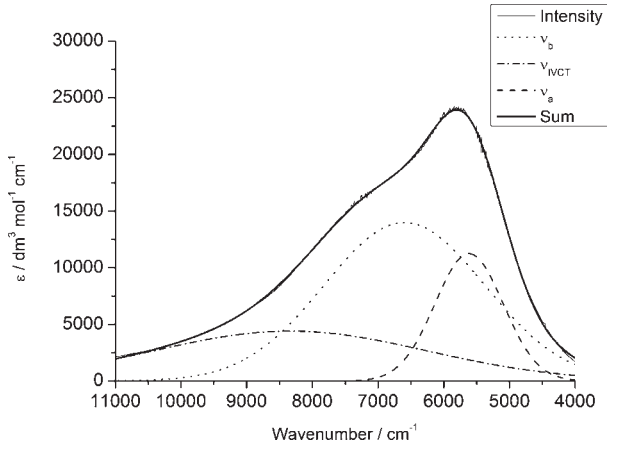

Figure 9. NIR region of the electronic spectrum of $[\mathbf{2}]^+$ showing deconvolution into a sum of three Gaussian-shaped bands.

the aromatic ring systems (Figure 7); similar distributions have been noted in the analogous iron complexes.[29] Regardless of the level of theory used (different basis sets and functionals), all computational efforts made for localizing the oxidation process to give rise to an asymmetric charge distribution failed, and symmetrical structures with density distributed both on the metals and the diethynylaromatic bridge were obtained in all cases. These 'symmetrical' calculated geometries are in good agreement with the expected distribution of electronic charge associated with a bridge-localized oxidation event in the experimental systems.

On the basis of these data summarized above, it can be concluded that the ground state electronic structure of each member of the series $[\mathbf{2}-\mathbf{5}]^{n+}$ features an appreciable contribution from the bridging ligand (Figure 2c). Similar 'bridge-centered' states have been described elsewhere, for example in the 9,10-diethynylanthracenyl-bridged bis(triarylamine) radical cation $[\mathbf{6}]^+$ (Chart 3),[63,64,86] and related ruthenium complexes derived from 1,4-diethynyl- and 1,4-divinylarylene based ligands.[51−53,91,92] The assignment of a bridge-localized ground state in the case of the ruthenium derivatives $[\mathbf{2}-\mathbf{5}]^+$ allows us to construct a qualitative representation of the adiabatic potential energy curve taken as a slice along a fixed asymmetric coordinate, which is similar to that described by Lambert for the 9,10-diethynylanthracenyl-bridged bis(triarylamine) radical cation $[\mathbf{6}]^+$ (Figure 8).[64] From this description of the prototypical 'bridge-localized' ground state two vertical electronic transitions with charge transfer character can be predicted, denoted ν_a and ν_b. Evolution of the first excited state along the asymmetric electron transfer coordinate leads to a double minimum, physically corresponding to the transfer of charge from one or other metal center to the bridge and hence a mixed-valence electronic structure in the excited state, while the second excited state surface is expected to feature only a single minimum. While under C_{2h} symmetry ν_b is forbidden, due to either vibrational coupling or local breaking of symmetry in solution these two transitions have been clearly resolved in the NIR spectra of the radical cation $[\mathbf{6}]^{+}$[64,67] and the bis(vinyl) complex $[\{RuCl(CO)(PMe_3)_3\}_2(\mu\text{-}1,4\text{-}CH{=}CHC_6H_4CH{=}CH)]^{+}$[92] in which the unpaired electron/hole is supported by the bridging moiety.

However, as noted above, the NIR absorption of $[\mathbf{2}-\mathbf{5}]^+$ can be deconvoluted into a sum of *three* Gaussian-shaped sub-bands (see Figure 9 for $[\mathbf{2}]^+$ and Table 3), although deconvolution of the anthracene derivative $[\mathbf{5}]^+$ must be treated with caution, since the NIR bands are significantly overlapped with the tail of the anthracene cation radical $\pi-\pi^*$ bands, which leads to a wider range of possible solutions to the deconvolution. Of these three observed transitions, only two can be attributed within the bridge-localized ground-state model and have MLCT character (Figure 8); i.e. photoexcitation in the NIR region results in formation of excited states with mixed-valence character from a bridge-localized ground state.[93] The introduction of the electron-donating methoxy groups stabilizes the unpaired electron on the bridge in **3** relative to **2** and raises the energy of the ν_a and ν_b transitions (Table 3). Similarly, the extension of the aromatic bridging moiety from phenylene to naphthylene to anthrylene also shifts the ν_a and ν_b bands to higher energy as the bridge-based ground state is stabilized.

The third transition is significantly broader than ν_a and ν_b and has a half-height bandwidth, $\Delta\nu_{1/2}$, that generally fits well with the predictions made on the basis of the Hush two-state model for weakly coupled mixed-valence systems,[94] and is relatively insensitive to the nature of the bridge (Table 3). The adiabatic potential energy curves derived from the three-state model in the limit of the bridging state being high in energy compared with the coupling between the remote centers (H_{AB}) is analytically similar to the two-state model.[18] This third component is therefore assigned to an intervalence charge transfer transition, ν_{IVCT}, with the assumption that, at the geometry associated with the mixed-valence form, the bridge state is considerably destabilized[4] and that the metal centers in the 'mixed-valence' state are only weakly coupled through the orbitals of the bridge.

To better understand and confirm the nature of the electronic transitions described above, time-dependent (TD) DFT calculations were carried out on **2-H** and $[\mathbf{2\text{-}H}]^+$ using the B3LYP functional, both with and without the application of the conductor-like polarizable continuum model (CPCM). Dichloromethane was chosen as solvent for these later computational investigations to reflect the experimental spectroelectrochemical conditions. The results from the neutral system **2-H** in vacuo and the main spectral features are reported in Table 4 and serve as a convenient starting point for the discussion.

Table 3. Selected Parameters Derived from Deconvolution of the NIR Absorption Band Envelope in $[2-5]^{+a}$

cmpd	$[2]^+$	$[3]^+$	$[4]^+$	$[5]^+$
ν_a/cm^{-1} (ε/M^{-1} cm^{-1})	5600 (11200)	6300 (15000)	6000 (9600)	6400 (9000)
ν_b/cm^{-1} (ε/M^{-1} cm^{-1})	6600 (14000)	7800 (8400)	7700 (5200)	8500 (6700)
ν_{IVCT}/cm^{-1} (ε/M^{-1} cm^{-1})	8300 (4400)	8500 (3400)	8300 (4900)	8100 (5000)
$\Delta(\nu_{IVCT})_{1/2}$[b]	4200	4000	4200	3000
$\Delta(\nu_{IVCT})_{1/2}$(calc)[c]	4380	4430	4380	4320

[a] Samples generated in a spectroelectrochemical cell from solutions in CH_2Cl_2/0.1 M NBu_4BF_4, with apparent molar absorption coefficients, ε. [b] $\Delta(\nu_{IVCT})_{1/2}$ is the observed half-height bandwidth of ν_{IVCT}. [c] $\Delta(\nu_{IVCT})_{1/2}(calc) = 2[4\ ln(2)\nu_{IVCT}RT]^{1/2} = [2310\nu_{IVCT}]^{1/2}$ at ambient temperature.[94]

Table 4. TD-DFT Characterization of Compound 2-H in Vacuo

λ/nm [cm^{-1}] ($f \times 10^3$)	main MO transitions	main assignement
471.5 [21210] (*5.1*)	HOMO→LUMO	bridge→metal (LMCT)
350.8 [28510] (*6.2*)	HOMO-2→ LUMO+3/HOMO-3→LUMO	metal-CC→metal (ML-LCT)
334.5 [29900] (*76.3*)	HOMO-1→LUMO+1/HOMO-1→LUMO	metal-CC→metal ML-LCT
325.5 [30720] (*1358*)	HOMO→LUMO+4/HOMO→LUMO+3	bridge $\pi-\pi^*$ admixed with LMCT

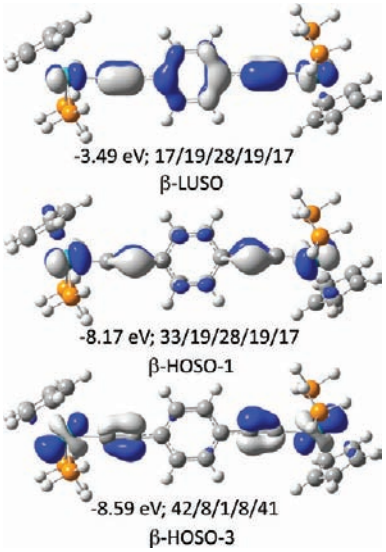

Figure 10. Selected frontier orbitals involved in the transition of the NIR band for the oxidized $[2\text{-}H]^+$ compound in solvent [contour values ± 0.04 $(e/b^3)^{1/2}$]. Orbital energies (eV) and composition [% Cp-$(PH_3)_2Ru/C_2/Ar/C_2/Ru(PH_3)_2Cp$] are summarized numerically.

The main absorption band calculated at 325.5 nm [30720 cm^{-1}] for **2-H** (cf. the experimentally observed band at 26810 cm^{-1} in **2**, Figure 5), arises from the diethynyl benzene $\pi-\pi^*$ transition (HOMO → LUMO+4) admixed with some LMCT (HOMO → LUMO+3) character (see Table S1, SI for orbital compositions). A small red-shift of ~25 nm is computed when the solvent is introduced, but the aryl−aryl transition character is maintained. The inclusion of a solvent model also results in some rearrangement in the electronic structure; in the model dichloromethane solution environment the diethynyl π^* orbital which comprises the LUMO+4 in vacuo is stabilized and found as the LUMO+2 in the CPCM calculation, with the consequence that the almost degenerate metal-based LUMO+2 and LUMO+3 (in vacuo) become the LUMO+3 and LUMO+4 in the solvated calculated system.

The $\pi-\pi^*$ band in $[2\text{-}H]^+$ is less intense and red-shifted (~65 nm) in comparison with the spectrum of **2-H**, and in addition a broad band appears in the NIR region at ~970 nm (in vacuo). The inclusion of the solvent in the simulated spectra leads to a red shift in the NIR band to 1175 nm in a better agreement with the experimental data. The nature of this NIR band (in solvent) was investigated in detail. Indeed, two electronic transitions close in energy are computed at 1175 nm [8510 cm^{-1}] (f = 0.540) and 1116.5 nm [8957 cm^{-1}] (f = 0.239). In both cases, the major contributions come from β-HOMO−1 → β-LUSO and β-HOMO−3 → β-LUSO (Figure10) and have largely ML-LCT character and can be assigned to the experimentally observed transitions, ν_a and ν_b However, no transition assignable to ν_{IVCT} was found using this model of $[2]^+$ in which oxidation takes place (largely) on the bridging ligand and therefore offers a symmetrical distribution of charge.

The observation of an IVCT transition (ν_{IVCT}) in addition to the bands ν_a and ν_b suggests that under the conditions of the experiment, the mixed-valence state is also appreciably thermally populated. Further, the good agreement between the shape of the IVCT band and that predicted from the two-state model indicates that in the mixed-valence geometry the bridge is largely decoupled from the metal centers. The coexistence of localized (mixed-valence state) and delocalized (bridge state) states in 4,4′-dinitrotolane radical anions has been noted recently, the relative populations of which were related to solvation factors.[95] In addition to the anomalous Mössbauer spectra of crystalline samples of $[1a]^+$, 'valence trapped' and 'valence detrapped' forms of various biferrocenium salts have also been observed, the form adopted being sensitive to the local crystalline environment.[96−99] In the case of the ruthenium complexes described here, the relative stability of the bridge-localized and mixed-valence states is likely to depend critically on the overlap of the metal d and aromatic bridging ligand π orbitals, and hence the angles ϕ_1 and ϕ_2 (i.e. the torsion angles defined by the plane of the aromatic portion of the bridging ligand relative to C(1)−Ru−C(0) at each metal center). When ϕ_1 and ϕ_2 are both close to 0°, the metal centers act as good donors, and the compounds are delocalized, with significant redox behavior associated with the bridge (see the discussion of the β-LUSO structure of $[2\text{-}H]^+$ and

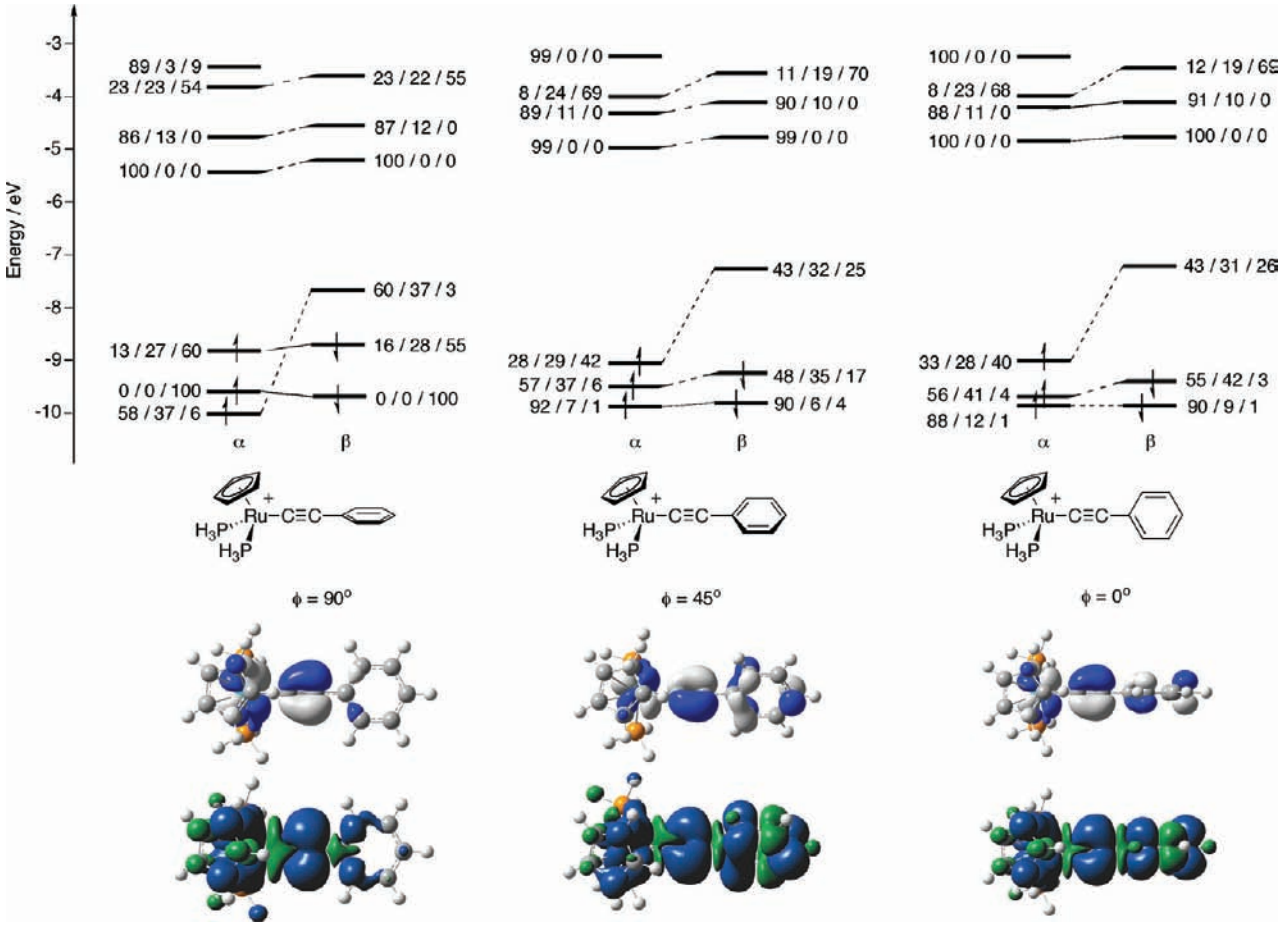

Figure 11. Plot of the energies (eV) and % composition $[Cp(PH_3)_2Ru/C{\equiv}C/C_6H_5]$ of selected α- and β-spin orbitals for the cation $[Ru(C{\equiv}CC_6H_5)(PH_3)_2Cp]^+$ calculated for values of ϕ constrained to 90°, 45°, and 0°. The lowest energy unoccupied β-SOs (isocontour ±0.04 $[e/b^3]^{1/2}$) and spin densities are also plotted (contour ±0.04 e/bohr^3).

$[\mathbf{5\text{-}H}]^+$ above). This is the situation modeled by the DFT calculations ($[\mathbf{2\text{-}H}]^+$ $\phi_1 = \phi_2 = 6.6°$; $[\mathbf{5\text{-}H}]^+$ $\phi_1 = 8.7°$, $\phi_2 = 8.8°$). For some values of $\phi_{1,2}$ one or both of the metal donors will decouple from the aromatic portion of the molecule, and the unpaired electron/hole will collapse onto the metal centers, giving rise to the mixed-valence state. The angular variation in spin density on metallic and arylalkynyl fragments in $[Fe(C{\equiv}CAr)(dppe)Cp^*]^+$ systems has been demonstrated computationally[100] and lends support to the general picture described above, while the role of bridge conformation on the magnitude of coupling between redox-active centers has been explored for, by way of example, bridges based on 4,4′-bipyridyl[101−103] and biphenylenes[32] among other examples.[33,34]

With a view to exploring the notion of the effect of the angle ϕ on the distribution of spin density in ruthenium systems, a series of calculations on the simple model $[Ru(C{\equiv}CC_6H_5)(PH_3)_2Cp]^+$ were undertaken for various angles ϕ. The $\phi = 0°$ conformation was optimized without constraint and has been reported and discussed in various contexts elsewhere,[68] while structures with $\phi = 45°$ and 90° were obtained by constraining the dihedral angle during the optimization. At the level of theory employed, the $\phi = 0°$ structure is the most stable, with the $\phi = 45°$ (ΔE = 1.6 kcal mol^{-1}) and the 90° (ΔE = 5.6 kcal mol^{-1}) structures lying higher in energy. Representative MO diagrams and plots of the β-LUSO and integrated spin density for these three different conformations are shown in Figure 11. There is relatively little variation in the composition or ordering of the unoccupied α-spin orbitals across the structural series, or in the nature of the unoccupied β-spin orbitals above the β-LUSO. However, the composition of the lowest unoccupied spin orbital (β-LUSO) varies more significantly with the angle ϕ with the greatest metallic character (60%) being found for the highest energy structure ($\phi = 90°$) and considerable aromatic ligand contribution being found in the case of the lowest energy ($\phi = 0°$) structure.[68] Thus, even for these simple models, the orientation of the phenyl acetylide ligand with respect to the highest occupied metal orbitals of the $Ru(PH_3)_2Cp$ fragment determines the extent to which the aromatic acetylide substituent can feature in stabilizing the unpaired electron/hole, which is further illustrated in the distribution of spin density across the molecular framework as a function of ϕ (Table 5 and Figure 11).

Returning to the bimetallic system it is possible to describe the ground-state potential energy surface in terms of an asymmetric (electron transfer) reaction coordinate and a rotational coordinate $X(\phi_1,\phi_2)$ that describes the relative conformation of the metal and bridge elements (Figure 12). Depending on the molecular conformation of the bimetallic complex, the lowest energy electronic configuration will place the charge on either the metals (states A and B in Figure 12) or bridge (state C, Figure 12) on the basis of the conformation-dependent spin density distribution

Table 5. Calculated Spin Densities (e) on Selected Atoms (or Sums of Groups of Atoms) for $[Ru(C{\equiv}CC_6H_5)(PH_3)_2Cp]^+$ Complexes for $\phi = 0°, 45°, 90°$

ϕ	Ru	ΣC_{Cp}	ΣP_{PH3}	C_α	C_β	C_i	C_o	C_m	C_p	ΔE (kcal mol^{-1})
0	0.419	0.040	0.007	0.026	0.284	−0.038	0.126, 0.125	−0.074, −0.073	0.179	0
45	0.426	0.032	0.004	0.033	0.290	−0.031	0.115, 0.116	−0.067, −0.067	0.167	+1.6
90	0.584	0.046	0.001	−0.068	0.441	−0.045	0.021, 0.022	−0.002, −0.002	0.005	+5.6

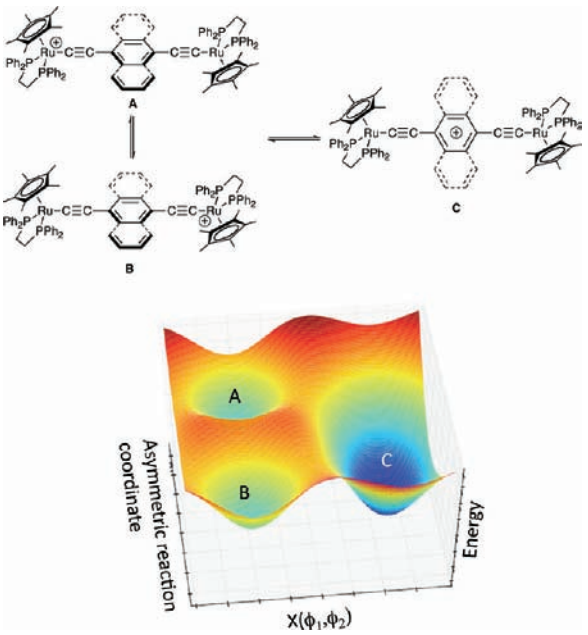

Figure 12. Sketch of the adiabatic ground-state potential energy surfaces shown in terms of an asymmetric electron transfer reaction coordinate Y and an angular reaction coordinate $X(\phi_1,\phi_2)$ describing the plane of the aromatic portion of the bridge relative to the Ru−C(0) vectors.

demonstrated for the mononuclear model system. Since the IVCT transition fits the Marcus−Hush two-state model well, it can be assumed that the bridge- and metal-localized states do not mix appreciably. For a fixed conformation, states A and B interconvert along the asymmetric reaction pathway, the trajectory of which maps the ground-state path in Figure 1a. Passage along the A−C or B−C trajectory corresponds to a change in molecular conformation, and at site C a slice along fixed $X(\phi_1,\phi_2)$ gives a 2-D single minimum ground-state surface shown in Figure 8.

To gain further insight into the nature of the radical cations $[\mathbf{2}-\mathbf{5}]^+$ and to provide further evidence for the proposed speciation in solution, we turned to IR spectroelectrochemical methods, to take advantage of the fast time resolution of vibrational spectroscopy and the characteristic shifts in ν(C≡C) frequencies that have proven to be diagnostic of metal and ligand redox state in previous studies of $[Ru(C{\equiv}CR)(PP)Cp']^{n+}$ complexes [(PP)Cp′ = $(PPh_3)_2Cp$; (dppe)Cp*].[22,50,68,104] The IR spectra of **2**−**5** are characterized by one (**2**−**4**) or two (**5**) ν(C≡C) bands arising from the symmetric and asymmetric stretching modes of the bridging ligand, the frequencies of which are similar to those of the analogous mononuclear complexes $[Ru(C{\equiv}CArH)(dppe)Cp^*]$[68] and reasonably well reproduced by the computational models (Table 6, Figure 13). Electrolysis in the IR cell gave a series of bands between 2100−1600 cm^{-1}, which are discussed in more detail below. Further electrolysis to the dications gave two, weak, low-frequency ν(CC) bands, arising from the symmetric and asymmetric stretches of the bridging ligand, which has significant quinoidal character in this charge state (vide supra). The frequencies of the dication ν(CC) bands are only a few wavenumbers lower than the ν(CC) bands found in related monocationic, mononuclear complexes $[Ru(C{\equiv}CR)(dppe)Cp^*]^+$.[68]

Given the description of the monocations in terms of the thermal population of both bridge and mixed-valence states proposed above, the IR spectra of $[\mathbf{2}-\mathbf{5}]^+$ deserve comment. For each member of the series $[\mathbf{2}-\mathbf{5}]^+$, four distinct features can be identified. Similar features in the IR spectra of closely related ruthenium complexes featuring diethynylarylene ligands have been noted elsewhere,[53] although the significance of the spectra has not been commented upon in detail. The frequency of the strongest ν(CC) band [1974 ($[\mathbf{2}]^+$); 1971 ($[\mathbf{3}]^+$); 1963 ($[\mathbf{4}]^+$); 1954 ($[\mathbf{5}]^+$) cm^{-1}] shows a dependence on the nature of the bridging moiety, and is broadened or split by symmetric and asymmetric components, a feature which is reproduced in the computational models. The symmetric component gains appreciable intensity through coupling to the MLCT electronic transitions. These vibrational features are assigned to the 'bridge-localized' ground state. Two weaker ν(CC) bands are also observed at frequencies close to those of $[Ru(C{\equiv}CR)(dppe)Cp^*]^{n+}$ (R = tolyl, naphthyl, anthryl; n = 0, 1) and resemble the two-band pattern observed for the nonconjugated derivative $[\{Ru(dppe)Cp^*\}_2(\mu\text{-}C{\equiv}CArC{\equiv}C)]^+$ (Ar = 1,3-C_6H_4) in which charge is asymmetrically distributed between the metal centers across the bridge.[50] These features, which are not modeled by the 'bridge-localized' DFT model, are assigned to the mixed-valence state. In addition, a ν(C═C) band from the aromatic portion of the bridge [1564 ($[\mathbf{2}]^+$); 1575 ($[\mathbf{3}]^+$); 1567 ($[\mathbf{4}]^+$); 1606 ($[\mathbf{5}]^+$) cm^{-1}] is also observed in each of $[\mathbf{2}-\mathbf{5}]^+$, but not the neutral or dicationic forms. This is consistent with the end-to-end dipole across the molecule in the localized mixed-valence state, and the coupling of this vibrational mode to the ν_b transition may be in part responsible for the intensity of this transition. The IR spectra are therefore consistent with the proposal of population of both bridge and mixed-valence states in solution.

CONCLUSIONS

Oxidation of $[\{Ru(dppe)Cp^*\}_2(\mu\text{-}C{\equiv}CArC{\equiv}C)]$ affords stable mono- and dications, the spectroscopic properties of which are consistent with a significant degree of C≡CArC≡C π-character in the frontier orbitals. In addition to the low-lying bridge state, the monocations also exhibit spectroscopic features in the NIR and IR regions consistent with the population of a mixed-valence state that lies close in energy to the bridge-state. The dicationic forms are best described in terms of quinoidal

Table 6. Summary of the IR Spectra of $[2-5]^{n+}$ (n = 0, 1, 2) Collected by in Situ Oxidation in a Spectroelectrochemical Cell (CH_2Cl_2/0.1M NBu_4BF_4)[a,b]

cmpd/charge, n	0 ν(C≡C)	1+ ν(C≡C)	1+ ν(aryl)	2+ ν(C≡C)
2	2068 (m)	2061 (w)	1564 (m)	1970 (vw)
		1997 (s)		1924 (w)
		1974 (vs)		
		1915 (w,sh)		
2-H[c]	2099 (562) asym	2021 (0.0) sym		1960 (4015) asym
	2093 (0.2) sym	2014 (6422) asym		1944 (0.0) asym
3	2060 (m)	2049 (w)	1575 (w)	1965 (w)
		1990 (m,sh)		1926 (m)
		1971 (vs)		
		1911 (w,sh)		
4	2051 (m)	2037 (w)	1567 (w)	1963 (vw)
		1995 (m,sh)		1912 (m)
		1963 (vs)		
		1915 (w,sh)		
5	2045 (m)	2020 (w)	1606 (w)	1951 (w)
	2031 (m)	1954 (vs)		1911 (m)
		1898 (w,sh)		
5-H[c]	2077 (911) asym	2017 (0.2) sym		1960 (1.0) sym
	2073 (0.0) sym	2004 (6206) asym		1958 (5692) asym
$[Ru(C{\equiv}CPh)(dppe)Cp^*]$[d]	2072 (s)	1929 (s)		
$[Ru(C{\equiv}CC_{10}H_7)(dppe)Cp^*]$[d]	2053 (s)	1916 (s)		
$[Ru(C{\equiv}CC_{14}H_9)(dppe)Cp^*]$[d]	2041 (s)	1925 (s)		

[a] Data from reference mononuclear complexes and the computational models $[\mathbf{2\text{-}H}]^{n+}$ and $[\mathbf{5\text{-}H}]^{n+}$ are given for comparison. [b] Calculated vibrational frequencies have been corrected by a factor of 0.95.[105,106] [c] Calculated models $[\mathbf{2\text{-}H}]^{+}$ and $[\mathbf{5\text{-}H}]^{+}$ correspond to the bridge-localized redox products. [d] From reference 68.

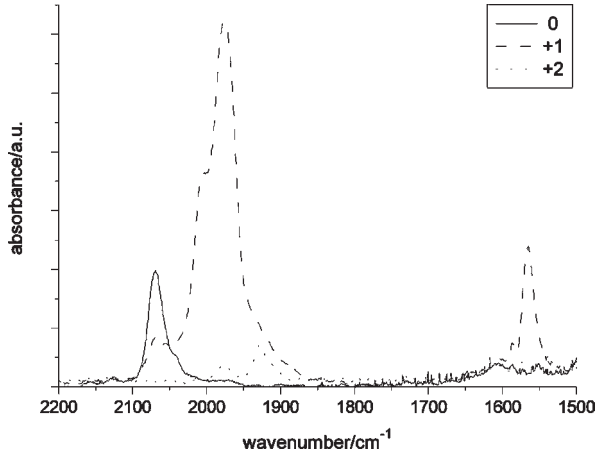

Figure 13. IR spectra collected by in situ oxidation of **2** to $[\mathbf{2}]^{+}$ and $[\mathbf{2}]^{2+}$ in a spectroelectrochemical cell (CH_2Cl_2/0.1 M NBu_4BF_4), which is representative of the series $[\mathbf{2-5}]^{n+}$.

resonance structures, stabilized by the strongly electron-donating metal centers. The simultaneous population of bridge and mixed-valence states is thought to be related to a number of factors that influence the relative stability of these states, including solvent environment and ion-pairing,[95] as well as orientation of the plane of the aromatic portion of the bridging ligand with respect to the metal d-orbitals of appropriate π-symmetry.[33,34,38] These additional environmental and mechanical factors serve to add further diversity to the landscape of behavior associated with open-shell bimetallic complexes $[\{ML_n\}(\mu\text{-bridge})\{ML_n\}]^{n\pm}$.

EXPERIMENTAL SECTION

General Conditions. All reactions were carried out under an atmosphere of nitrogen using standard Schlenk techniques. Reaction solvents were purified and dried using an Innovative Technology SPS-400, and degassed before use. No special precautions were taken to exclude air or moisture during workup. The precursors, $[RuCl(dppe)Cp^*]$,[87] $Me_3SiC{\equiv}CC_6H_2(OMe)_2C{\equiv}CSiMe_3$, 1,4-bis(trimethylsilylethynyl)naphthalene, and 9,10-bis(trimethylsilylethynyl)anthracene,[107] and complex **2**[51] were prepared by literature routes. Other reagents were purchased and used as received.

The NMR spectra were recorded on a 400 MHz Bruker Avance spectrometer from deuterated chloroform or benzene solutions and were referenced against residual protio solvent resonances ($CHCl_3$: ^{1}H 7.26 ppm, ^{13}C 77.0 ppm; C_6HD_5: ^{1}H 7.15 ppm, ^{13}C 128.0 ppm) or external phosphoric acid. IR spectra were recorded using a Nicolet Avatar spectrometer from Nujol mull suspended between NaCl plates or from KBr discs. Electrospray ionization mass spectra were recorded using Thermo Quest Finnigan Trace MS-Trace GC or WATERS Micromass LCT spectrometers. Samples in dichloromethane (1 mg/mL) were 100 times diluted in either methanol or acetonitrile and analyzed with source and desolvation temperatures both of 120 °C, with cone voltage of 30 V.

Electrochemical analyses were carried out using an EcoChemie Autolab PG-STAT 30 potentiostat, with platinum working electrode, a counterelectrode, and a platinum wire counterelectrode, and a platinum wire pseudo-reference electrode, from solutions in CH_2Cl_2 containing

0.1 M NBu_4BF_4 electrolyte, ν = 100 mV s^{-1}. The ferrocene/ferrocenium couple was used as an internal reference for potential measurements such that the FcH/FcH^+ couple falls at 0.46 V vs SCE.[108] Spectroelectrochemical measurements were made in an OTTLE cell of Hartl design,[109] from CH_2Cl_2 solutions containing 0.1 M NBu_4BF_4 electrolyte. The cell was fitted into the sample compartment of a Nicolet Avatar FT-IR or a Perkin-Elmer Lambda 900 UV−vis−NIR spectrophotometer, and electrolysis in the cell was performed with a home-built potentiostat.

Preparation of [{Ru(dppe)Cp*}$_2$(μ-C≡CC$_6$H$_2$(OMe)$_2$C≡C)] (3). A suspension of [RuCl(dppe)Cp*] (200 mg, 0.299 mmol), $Me_3SiC{\equiv}CC_6H_2(OMe)_2C{\equiv}CSiMe_3$ (44 mg, 0.133 mmol), and KF (100 mg, 1.72 mmol) in dry degassed methanol (20 mL) was heated at reflux for 18 h under a nitrogen atmosphere. After cooling, three drops of DBU were added to the reaction mixture, and the mixture was allowed to stir at RT for an hour. The sandy brown precipitate formed was filtered. The solid was dissolved in dichloromethane and precipitated from slow diffusion with hexane. The solid was filtered and dried to give **3** as a light-brown powder (130 mg, 0.089 mmol, 67%). Crystals suitable for X-ray crystallography were grown from slow diffusion of methanol into a dichloromethane solution of **3**. IR (Nujol): ν(C≡C) 2061 cm^{-1}. ^{1}H NMR (C_6D_6, 400 MHz): δ 1.69 (s, 30H, Cp*); 1.99 (m, 4H, CH_2); 2.92 (m, 4H, CH_2); 3.43 (s, 6H, OCH_3), 6.64 (s, 2H, CH C_6H_2), 7.02 (m, 16H, *meta* and *para* CH dppe), 7.12 (m, 8H, *meta* CH dppe), 7.16 (m, 8H, *ortho* CH dppe), 7.99 (m, 8H, *ortho* CH dppe). ^{1}H NMR ($CDCl_3$, 400 MHz): δ 1.57 (s, 30H, Cp*); 2.14 (m, 4H, CH_2); 2.84 (m, 4H, CH_2); 3.42 (br s, 6H, OCH_3), 6.17 (s, 2H, C_6H_2), 7.11 (m, 8H, CH dppe), 7.23 (m, 8H, CH dppe), 7.28 (m, 16H, CH dppe), 7.84 (m, 8H, *ortho* CH dppe). ^{31}P{^{1}H} NMR (C_6D_6, 81 MHz): δ 82.3 (s, dppe). ^{31}P{^{1}H} NMR ($CDCl_3$, 81 MHz): δ 82.2 (br s, dppe). ES(+)-MS (*m*/*z*):1453 [{Ru(dppe)Cp*}$_2$(μ-C≡CC$_6$H$_2$(OMe)$_2$C≡C)].

Preparation of [{Ru(dppe)Cp*}$_2$(μ-C≡CC$_{10}$H$_6$C≡C)] (4). A suspension of [RuCl(dppe)Cp*] (200 mg, 0.299 mmol), $Me_3SiC{\equiv}CC_{10}H_6C{\equiv}CSiMe_3$ (48 mg, 0.151 mmol), and KF (35 mg, 0.60 mmol) in methanol (20 mL) was heated to reflux under a nitrogen atmosphere for 90 min. The yellow precipitate formed was collected, washed with methanol and hexane, and dried to give **4** as a yellow powder (135 mg, 0.0935 mmol, 63%). IR (Nujol): ν(C≡C) 2055 cm^{-1}. ^{1}H NMR (C_6D_6, 400 MHz): δ 1.67 (s, 30H, Cp*); 1.90 (m, 4H, CH_2); 2.77 (m, 4H, CH_2); 7.02 (m, 16H, *meta* and *para* CH dppe), 7.08 (s, 2H, CH $C_{10}H_6$), 7.12 (m, 8H, *meta* CH dppe), 7.18 (dd, 2H, CH $C_{10}H_6$), 7.20 (m, 8H, *ortho* CH dppe), 7.90 (m, 8H, *ortho* CH dppe), 8.19 (dd, 2H, CH $C_{10}H_6$).^{31}P{^{1}H} NMR (C_6D_6, 81 MHz): δ 82.4 (s, dppe). ^{13}C{^{1}H} NMR (C_6D_6, 126 MHz): δ 10.5 (s, C_5Me_5), 29.7 (m, CH_2), 92.8 (s, C_5Me_5), 110.1 (s, C≡$\underline{C}$C$_{10}$H$_6$), 124.5, 124.6 (CH in $C_{10}H_6$); 128.2 (CH); 128.5; 130.0 (CH); 131.9 (C1−C4); 129.1, 128.9 ($C_{p,p'}$); 133.7, 134.3 (dds, $J_{CP/CCP} \approx 5$ Hz, $C_{o,o'}$); 135.2 (CH in $C_{10}H_6$), 137.7, 139.6 (m, $C_{i,i'}$). The $C_{m,m'}$ dppe peak is assumed to be hidden by the C_6D_6 peak. The weak Ru−C and two C peaks of $C_{10}H_6$ were not observed. ES(+)-MS (*m*/*z*): 1444 [{Ru(dppe)Cp*}$_2$(μ-C≡CC$_{10}$H$_6$C≡C)].

Preparation of [{Ru(dppe)Cp*}$_2$(μ-C≡CC$_{14}$H$_8$C≡C)] (5). A suspension of [RuCl(dppe)Cp*] (500 mg, 0.747 mmol), $Me_3SiC{\equiv}CC_{14}H_8C{\equiv}CSiMe_3$ (140 mg, 0.374 mmol), and KF (100 mg, 1.72 mmol) were treated with methanol (40 mL), and the suspension formed was heated at reflux for 40 h under a nitrogen atmosphere. The red precipitate formed was collected and washed with MeOH and hexane and dried to give **5** as a red/purple powder (451 mg, 0.302 mmol, 81%). IR (Nujol): ν(C≡C) 2029 cm^{-1}. ^{1}H NMR (C_6D_6, 400 MHz): δ 1.72 (s, 30H, Cp*); 1.99 (m, 4H, CH_2); 2.97 (m, 4H, CH_2); 6.95 (dd, 2H, CH $C_{10}H_6$), 7.02 (m, 16H, *meta* and *para* CH dppe), 7.08 (s, 2H, CH $C_{10}H_6$), 7.12 (m, 8H, *meta* CH dppe), 7.18 (m, 8H, *ortho* CH dppe), 7.85 (m, 8H, *ortho* CH dppe), 8.25 (dd, 2H, CH $C_{10}H_6$). ^{31}P{^{1}H} NMR (C_6D_6, 81 MHz): δ 82.8 (s, dppe). ES(+)-MS (*m*/*z*): 1494[{Ru(dppe)Cp*}$_2$(μ-C≡CC$_{14}$H$_8$C≡C)].

Crystallography. Single-crystal X-ray data were collected on a Bruker SMART 6000 diffractometer equipped with a Cryostream (Oxford Cryosystems) nitrogen cooling device at 120 K and 250 K for **3** and **5**, respectively, using graphite monochromated Mo K_α radiation (λ = 0.71073 Å). The structures were solved by direct method and refined by full-matrix least-squares on F^2 for all data using SHELXTL software.[110] All nondisordered non-hydrogen atoms were refined with anisotropic displacement parameters, H atoms were placed in the calculated positions and refined in riding mode. Crystallographic data for the structures have been deposited with the Cambridge Crystallographic Data Centre as supplementary publications CCDC-839623 and 839624.

Crystal data for 3. $C_{84}H_{86}O_2P_4Ru_2$, M = 1453.55, monoclinic, space group $P2_1/n$, a = 12.2385(3) Å, b = 22.4341(5) Å, c = 13.0592(3) Å, β = 99.02(1)°, U = 3541.1(2) Å^3, $F(000)$ = 1508, Z = 2, D_c = 1.363 mg m^{-3}, μ = 0.565 mm^{-1}. 51638 reflections ($1.82 \le \theta \le 31.50°$) were collected ($\omega$-scan, 0.3°/frame) yielding 11778 unique data (R_{merg} = 0.0269). Final $wR_2(F^2)$ = 0.0819 for all data (419 refined parameters), conventional $R_1(F)$ = 0.0302 for 10029 reflections with $I \ge 2\sigma$, GOF = 1.041.

Crystal data for 5. $C_{90}H_{86}Ru_2P_4 \times 5\ C_6H_6$, M = 1884.15, triclinic, space group $P\bar{1}$, a = 11.9292(12) Å, b = 13.7023(13) Å, c = 17.4694(17) Å, α = 98.876(3), β = 101.348(3)°, γ = 114.727(4)°, U = 2451.6(4) Å^3, $F(000)$ = 984, Z = 1, D_c = 1.276 mg m^{-3}, μ = 0.423 mm^{-1}. 20000 reflections were collected (ω-scan, 0.3°/frame) yielding 13127 unique data (R_{merg} = 0.0752). Final $wR_2(F^2)$ = 0.2410 for all data (499 refined parameters), conventional $R_1(F)$ = 0.0769 for 6381 reflections with $I \ge 2\sigma$, GOF = 0.993.

Computational Details. All DFT computations were carried out with the Gaussian 03 package.[111] The model geometries of the dinuclear systems $[\mathbf{2}\text{-}\mathbf{H}]^{n+}$ and $[\mathbf{5}\text{-}\mathbf{H}]^{n+}$ (n = 0, 1, 2) discussed here were optimized at the B3LYP/3-21G* level of theory,[112−115] to reduce computational effort, with no symmetry constraints. Test calculations performed at a higher level of theory with a B3LYP/LANL2DZ basis set with polarization functions on all elements lead to comparable results, in a manner similar to that reported elsewhere.[68] MOs and frequencies were computed on these optimized geometries at the same level of theory. All geometries were identified as minima (no imaginary frequencies). A scaling factor of 0.95 was applied to the calculated frequencies.[105,106] The MO contributions were generated using the GaussSum package and plotted using GaussView 5.0.[116] TD-DFT calculations were carried out on **2**-**H** and $[\mathbf{2}\text{-}\mathbf{H}]^+$ at the B3LYP/3-21G* level with and without the application of the conductor-like polarizable continuum model (CPCM)[117] to address or not address solvation effects, respectively.

■ ASSOCIATED CONTENT

Supporting Information. Complete refs 88 and 111. Plots of the IR and UV−vis−NIR spectra of $[\mathbf{2}-\mathbf{5}]^{n+}$ (n = 0, 1, 2). Plots showing the deconvolution of the NIR spectra of $[\mathbf{2}-\mathbf{5}]^+$. Complete references 88 and 111. Crystallographic data in cif format. Tables of energy and composition of selected molecular orbitals for $[\mathbf{2}\text{-}\mathbf{H}]^{n+}$ and $[\mathbf{5}\text{-}\mathbf{H}]^{n+}$ (n = 0, 1, 2). Cartesian coordinates of optimized geometries and energies of $[\mathbf{2}\text{-}\mathbf{H}]^{n+}$ and $[\mathbf{5}\text{-}\mathbf{H}]^{n+}$ (n = 0, 1, 2). Cartesian coordinates and energies of [Ru(C≡CPh)-$(PH_3)_2$Cp] in three configurations. Theis material is available free of charge via the Internet at http://pubs.acs.org.

■ AUTHOR INFORMATION

Corresponding Author
p.j.low@durham.ac.uk.

■ ACKNOWLEDGMENT

This work was supported by the EPSRC through award of a Leadership Fellowship to P.J.L.; R.L.R. held a PhD scholarship from the Durham Doctoral Training Account; and J.-F.H., B.L. G., and P.J.L. acknowledge the CNRS (France) for travel grants (PICS program). Part of this work was conducted in the scope of the CNRS Associated European Laboratory "Molecular Materials and Catalysis (MMC)" involving the Department of Chemistry of Durham University and the Laboratoire des Sciences Chimiques de Rennes.

■ REFERENCES

(1) Geiger, W. E.; Barriere, F. *Acc. Chem. Res.* **2010**, *43*, 1030.
(2) Lu, Y. H.; Quardokus, R.; Lent, C. S.; Justard, F.; Lapinte, C.; Kandel, S. A. *J. Am. Chem. Soc.* **2010**, *132*, 13519.
(3) Guo, S.; Kandel, S. A. *J. Phys. Chem. Lett.* **2010**, *1*, 420.
(4) Creutz, C. *Prog. Inorg. Chem.* **1983**, *30*, 1.
(5) Nocera, D. G. *Inorg. Chem.* **2009**, *48*, 10001.
(6) Aguirre-Etcheverry, P.; O'Hare, D. *Chem. Rev.* **2010**, *110*, 4839.
(7) Low, P. J.; Brown, N. J. *J. Cluster Sci.* **2010**, *21*, 235.
(8) Glover, S. D.; Goeltz, J. C.; Lear, B. J.; Kubiak, C. P. *Coord. Chem. Rev.* **2010**, *254*, 331.
(9) Paul, F.; Lapinte, C. *Coord. Chem. Rev.* **1998**, *178*, 431.
(10) (a) Low, P. J. *Dalton Trans.* **2005**, 2821. (b) Akita, M.; Koike, T. *Dalton Trans.* **2008**, 3523.
(11) Kim, B.; Beebe, J. M.; Olivier, C.; Rigaut, S.; Touchard, D.; Kushmerick, J. G.; Zhu, X. Y.; Frisbie, C. D. *J. Phys. Chem. C* **2007**, *111*, 7521.
(12) Liu, Y. F.; Lagrost, C.; Costuas, K.; Tchouar, N.; Le Bozec, H.; Rigaut, S. *Chem. Commun.* **2008**, 6117.
(13) Mahapatro, A. K.; Ying, J. W.; Ren, T.; Janes, D. B. *Nano Lett.* **2008**, *8*, 2131.
(14) Ying, J.-W.; Liu, I.P.-C.; Xi, B.; Song, Y.; Campana, C.; Zuo, J.-L.; Ren, T. *Angew. Chem., Int. Ed.* **2010**, *49*, 954.
(15) Liu, K.; Wang, X. H.; Wong, F. S. *ACS Nano* **2008**, *2*, 2315.
(16) Terada, K.; Kobayashi, K.; Hikita, J.; Haga, M. *Chem. Lett.* **2009**, *38*, 416.
(17) Tuccitto, N.; Ferri, V.; Cavazzini, M.; Quici, S.; Zhavnerko, G.; Licciardello, A.; Rampi, M. A. *Nat. Mater.* **2009**, *8*, 41.
(18) Brunschwig, B. S.; Creutz, C.; Sutin, N. *Chem. Soc. Rev.* **2002**, *31*, 168.
(19) D'Alessandro, D. M.; Keene, F. R. *Chem. Soc. Rev.* **2006**, *35*, 424.
(20) Roué, S.; Lapinte, C.; Bataille, T. *Organometallics* **2004**, *23*, 2558.
(21) Hamon, P.; Justaud, F.; Cador, O.; Hapiot, P.; Rigaut, S.; Toupet, L.; Ouahab, L.; Stueger, H.; Hamon, J. R.; Lapinte, C. *J. Am. Chem. Soc.* **2008**, *130*, 17372.
(22) Fox, M. A.; Roberts, R. L.; Baines, T. E.; Le Guennic, B.; Halet, J.-F.; Hartl, F.; Yufit, D. S.; Albesa-Jové, D.; Howard, J. A. K.; Low, P. J. *J. Am. Chem. Soc.* **2008**, *130*, 3566.
(23) Brown, N. J.; Lancashire, H. N.; Fox, M. A.; Collison, D.; Edge, R.; Yufit, D. S.; Howard, J. A. K.; Whiteley, M. W.; Low, P. J. *Organometallics* **2011**, *30*, 884.
(24) (a) Paul, F.; Bondon, A.; da Costa, G.; Malvolti, F.; Sinbandhit, S.; Cador, O.; Costuas, K.; Toupet, L.; Boillot, M.-L. *Inorg. Chem.* **2009**, *48*, 10608. (b) Paul, F.; Toupet, L.; Thépot, J.-Y.; Costuas, K.; Halet, J.-F.; Lapinte, C. *Organometallics* **2005**, *24*, 5464. (c) Costuas, K.; Paul, F.; Toupet, L.; Halet, J.-F.; Lapinte, C. *Organometallics* **2004**, *23*, 2053.
(25) Le Narvor, N.; Lapinte, C. *Organometallics* **1995**, *14*, 634.
(26) Weyland, T.; Lapinte, C.; Frapper, G.; Calhorda, M. J.; Halet, J.-F.; Toupet, L. *Organometallics* **1997**, *16*, 2024.
(27) For studies on closely related systems, see (a) Medei, L.; Orian, L.; Semeikin, O. V.; Peterleitner, M. G.; Ustynyuk, N. A.; Santi, S.; Durante, C.; Ricci, A.; Lo Sterzo, C. *Eur. J. Inorg. Chem.* **2006**, *13*, 2582. (b) Matsuura, Y.; Tanaka, Y.; Akita, M. *J. Organomet. Chem.* **2009**, *694*, 1840.
(28) Tanaka, Y.; Shaw-Taberlet, J. A.; Justaud, F.; Cador, O.; Roisnel, T.; Akita, M.; Hamon, J. R.; Lapinte, C. *Organometallics* **2009**, *28*, 4656.
(29) de Montigny, F.; Argouarch, G.; Costuas, K.; Halet, J.-F.; Roisnel, T.; Toupet, L.; Lapinte, C. *Organometallics* **2005**, *24*, 4558.
(30) Ibn Ghazala, S.; Paul, F.; Toupet, L.; Roisnel, T.; Hapiot, P.; Lapinte, C. *J. Am. Chem. Soc.* **2006**, *128*, 2463.
(31) D'Alessandro, D. M.; Keene, F. R. *Pure Appl. Chem.* **2008**, *80*, 1.
(32) Benniston, A. C.; Harriman, A.; Li, P.; Sams, C. A.; Ward, M. D. *J. Am. Chem. Soc.* **2004**, *126*, 13630.
(33) Chisholm, M. H.; Feil, F.; Hadad, C. M.; Patmore, N. J. *J. Am. Chem. Soc.* **2005**, *127*, 18150.
(34) Romanczyk, P. P.; Noga, K.; Wlodarczyk, A. J.; Nitek, W.; Broclawik, E. *Inorg. Chem.* **2010**, *49*, 7676.
(35) Otón, F.; Ratera, I.; Espinosa, A.; Tárranga, A.; Veciana, J.; Molina, P. *Inorg. Chem.* **2010**, *49*, 3183.
(36) Olivier, C.; Costuas, K.; Choua, S.; Maurel, V.; Turek, P.; Saillard, J.-Y.; Touchard, D.; Rigaut, S. *J. Am. Chem. Soc.* **2010**, *132*, 5638.
(37) Lear, B. J.; Chisholm, M. H. *Inorg. Chem.* **2009**, *48*, 10954.
(38) Chisholm, M. H.; Lear, B. J.; Moscatelli, A.; Peteanu, L. A. *Inorg. Chem.* **2010**, *49*, 3706.
(39) Fitzgerald, E. C.; Ladjarafi, A.; Brown, N. J.; Collison, D.; Costuas, K.; Edge, R.; Halet, J.-F.; Justaud, F.; Low, P. J.; Meghezzi, H.; Roisnel, T.; Whiteley, M. W.; Lapinte, C. *Organometallics* **2011**, *30*, 4180.
(40) The effect of the relative disposition of metal and aryl-ethynyl ligand fragments on the distribution of electron spin density in related mono-metallic $M(C{\equiv}CAr)L_n$ systems has also been noted: Paul, F.; Malvolti; da Costa, G.; Le Stang, S.; Justaud, F.; Argouarch, G.; Bondon, A.; Sinbandhit, S.; Costuas, K.; Toupet, L.; Lapinte, C. *Organometallics* **2010**, *29*, 2491.
(41) Kaim, W.; Schwederski, B. *Coord. Chem. Rev.* **2010**, *254*, 1580.
(42) Záliš, S.; Winter, R. F.; Kaim, W. *Coord. Chem. Rev.* **2010**, *254*, 1383.
(43) Lever, A. B. P. *Coord. Chem. Rev.* **2010**, *254*, 1397.
(44) Pevney, F.; Winter, R. F.; Sarkar, B.; Záliš, S. *Dalton Trans.* **2010**, *39*, 8000.
(45) Das, A. K.; Sarkar, B.; Fiedler, J.; Záliš, S.; Hartenbach, I.; Strobel, S.; Lahiri, G. K.; Kaim, W. *J. Am. Chem. Soc.* **2009**, *131*, 8895.
(46) Ghumaan, S.; Sarkar, B.; Maji, S.; Puranik, V. G.; Fiedler, J.; Urbanos, F. A.; Jimenez-Aparicio, R.; Kaim, W.; Lahiri, G. K. *Chem.—Eur. J.* **2008**, *14*, 10816.
(47) Maurer, J.; Linseis, M.; Sarkar, B.; Schwederski, B.; Niemeyer, M.; Kaim, W.; Záliš, S.; Anson, C.; Zabel, M.; Winter, R. F. *J. Am. Chem. Soc.* **2008**, *130*, 259.
(48) Linseis, M.; Winter, R. F.; Sarkar, B.; Kaim, W.; Záliš, S. *Organometallics* **2008**, *27*, 3321.
(49) Maji, S.; Sarkar, B.; Mobin, S. M.; Fiedler, J.; Kaim, W.; Lahiri, G. K. *Dalton Trans.* **2007**, 2411.
(50) Fox, M. A.; Farmer, J. D.; Roberts, R. L.; Humphrey, M. G.; Low, P. J. *Organometallics* **2009**, *28*, 5266.
(51) Armitt, D. J.; Bruce, M. I.; Gaudio, M.; Zaitseva, N. N.; Skelton, B. W.; White, A. H.; Le Guennic, B.; Halet, J.-F.; Fox, M. A.; Roberts, R. L.; Hartl, F.; Low, P. J. *Dalton Trans.* **2008**, 6763.
(52) Launay, J.-P.; Coudret, C.; Hortholary, C. *J. Phys. Chem. B* **2007**, *111*, 6788.
(53) Klein, A.; Lavastre, O.; Fiedler, J. *Organometallics* **2006**, *25*, 635.
(54) Ward, M. D.; McCleverty, J. A. *J. Chem. Soc., Dalton Trans.* **2002**, 275.
(55) Ernst, S.; Hänel, P.; Jordanov, J.; Kaim, W.; Kasack, V. *J. Am. Chem. Soc.* **1989**, *111*, 1733.
(56) Kaim, W.; Kasack, V. *Inorg. Chem.* **1990**, *29*, 4696.
(57) Piepho, S. B.; Krausz, E. R.; Schatz, P. N. *J. Am. Chem. Soc.* **1978**, *100*, 2996.
(58) Ondrenchen, M. J.; Ko, J.; Zhang, L. T. *J. Am. Chem. Soc.* **1987**, *109*, 1672.
(59) Ko, J.; Ondrechen, M. J. *J. Am. Chem. Soc.* **1985**, *107*, 6161.
(60) Root, L. R.; Ondrechen, M. J. *Chem. Phys. Lett.* **1982**, *93*, 421.

(61) Borshch, S. A.; Kotov, I. N.; Bersuker, I. B. *Chem. Phys. Lett.* **1982**, *89*, 381.
(62) Launay, J.-P.; Coudret, C.; Hortholary, C. *J. Phys. Chem. B* **2007**, *111*, 6788.
(63) Lambert, C.; Noll, G.; Schelter, J. *Nat. Mater.* **2002**, *1*, 69.
(64) Lambert, C.; Amthor, S.; Schelter, J. *J. Phys. Chem. A* **2004**, *108*, 6474.
(65) Amthor, S.; Lambert, C. *J. Phys. Chem. A* **2006**, *110*, 1177.
(66) Amthor, S.; Lambert, C.; Dummier, S.; Fischer, I.; Schelter, J. *J. Phys. Chem. A* **2006**, *110*, 5204.
(67) Seibt, J.; Schaumlöffel, A.; Lambert, C.; Engel, V. *J. Phys. Chem. A* **2008**, *112*, 10178.
(68) (a) Fox, M. A.; Roberts, R. L.; Khairul, W. M.; Hartl, F.; Low, P. J. *J. Organomet. Chem.* **2007**, *692*, 3277. (b) Bruce, M. I.; Burgun, A.; Gendron, F.; Grelaud, G.; Halet, J.-F.; Skelton, B. W. *Organometallics* **2011**, *30*, 2861.
(69) (a) Paul, F.; Ellis, B. G.; Bruce, M. I.; Toupet, L.; Roisnel, T.; Costuas, K.; Halet, J.-F.; Lapinte, C. *Organometallics* **2006**, *25*, 649. (b) Khairul, W. M.; Fox, M. A.; Zaitseva, N. N.; Gaudio, M.; Yufit, D. S.; Skelton, B. W.; White, A. H.; Howard, J. A. K.; Bruce, M. I.; Low, P. J. *Dalton Trans.* **2009**, 610. (c) Bruce, M. I.; Costuas, K.; Davin, T.; Ellis, B. G.; Halet, J.-F.; Lapinte, C.; Low, P. J.; Smith, M. E.; Skelton, B. W.; Toupet, L.; White, A. H. *Organometallics* **2005**, *24*, 3864. (d) Maurer, J.; Linseis, M.; Sarkar, B.; Schwederski, B.; Niemeyer, M.; Kaim, W.; Záliš, S.; Anson, C.; Zabel, M.; Winter, R. F. *J. Am. Chem. Soc.* **2007**, *130*, 259. (e) Costuas, K.; Rigaut, S. *Dalton Trans.* **2011**, *40*, 5643.
(70) Khan, M. S.; Kakkar, A. K.; Igham, S. L.; Raithby, P. R.; Lewis, J.; Spencer, B.; Wittmann, F.; Friend, R. H. *J. Organomet. Chem.* **1994**, *472*, 247.
(71) Beljonne, D.; Colbert, M. C. B.; Raithby, P. R.; Friend, R. H.; Bredas, J. L. *Synth. Met.* **1996**, *81*, 179.
(72) Lavastre, O.; Plass, J.; Bachmann, P.; Guesmi, S.; Moinet, C.; Dixneuf, P. H. *Organometallics* **1997**, *16*, 184.
(73) Colbert, M. C. B.; Lewis, J.; Long, N. J.; Raithby, P. R.; Younus, M.; White, A. J. P.; Williams, D. J.; Payne, M. M.; Yellowlees, L.; Beljonne, D.; Chawdhury, N.; Friend, R. H. *Organometallics* **1998**, *17*, 3034.
(74) Hurst, S. K.; Cifuentes, M. P.; McDonagh, A. M.; Humphrey, M. G.; Samoc, M.; Luther-Davies, B.; Asselberghs, I.; Persoons, A. *J. Organomet. Chem.* **2002**, *642*, 259.
(75) Hurst, S.; Ren, T. *J. Organomet. Chem.* **2002**, *660*, 1.
(76) Gao, L.-B.; Zhang, L.-Y.; Shi, L.-X.; Chen, Z.-N. *Organometallics* **2005**, *24*, 1678.
(77) Samoc, M.; Gauthier, N.; Cifuentes, M. P.; Paul, F.; Lapinte, C.; Humphrey, M. G. *Angew. Chem., Int. Ed.* **2006**, *45*, 7376.
(78) Gao, L.-B.; Kan, J.; Fan, Y.; Zhang, L.-Y.; Liu, S.-H.; Chen, Z.-N. *Inorg. Chem.* **2007**, *46*, 5651.
(79) Olivier, C.; Kim, B. S.; Touchard, D.; Rigaut, S. *Organometallics* **2008**, *27*, 509.
(80) Gauthier, N.; Olivier, C.; Rigaut, S.; Touchard, D.; Roisnel, T.; Humphrey, M. G.; Paul, F. *Organometallics* **2008**, *27*, 1063.
(81) Gauthier, N.; Argouarch, G.; Paul, F.; Humphrey, M. G.; Toupet, L.; Ababou-Girard, S.; Sabbah, H.; Hapiot, P.; Fabre, B. *Adv. Mater.* **2008**, *20*, 1952.
(82) Hu, W. Y.; Jia, G. *Can. J. Chem.* **2009**, *87*, 134.
(83) Field, L. D.; Magill, A. M.; Shearer, T. K.; Colbran, S. B.; Lee, S. T.; Dalgarno, S. J.; Bhadbhade, M. M. *Organometallics* **2010**, *29*, 957.
(84) Pevny, F.; Di Piazza, E.; Norel, L.; Drescher, M.; Winter, R. F.; Rigaut, S. *Organometallics* **2010**, *29*, 5912.
(85) Bruce, M. I.; Hall, B. C.; Kelly, B. D.; Low, P. J.; Skelton, B. W.; White, A. H. *J. Chem. Soc., Dalton Trans.* **1999**, 3719.
(86) Lambert, C.; Risko, C.; Coropceanu, V.; Schelter, J.; Amthor, S.; Gruhn, N. E.; Durivage, J. C.; Bredas, J.-L. *J. Am. Chem. Soc.* **2005**, *127*, 8508.
(87) Bruce, M. I.; Ellis, B. G.; Low, P. J.; Skelton, B. W.; White, A. H. *Organometallics* **2003**, *22*, 3184.
(88) Khan, M. S.; et al. *New. J. Chem.* **2003**, *27*, 140.
(89) Bruce, M. I.; Head, N. J.; Skelton, B. W.; White, A. H. *Acta Crystallogr., Sect. C: Cryst. Struct. Commun.* **2004**, *60*, o60.
(90) Liu, A.; Sauer, M. C., Jr.; Loffredo, D. M.; Trifunac, A. D. *J. Photochem. Photobiol. A* **1992**, *67*, 197.
(91) Maurer, J.; Sarkar, B.; Kaim, W.; Winter, R. F.; Záliš, S. *Chem.—Eur. J.* **2007**, *13*, 10257.
(92) Man, W. Y.; Xia, J.-L.; Brown, N. J.; Farmer, J. D.; Yufit, D. S.; Howard, J. A. K.; Liu, S. H.; Low, P. J. *Organometallics* **2011**, *30*, 1852.
(93) For a discussion of related transitions in closed shell donor-B-donor systems see reference 66.
(94) Creutz, C. *Prog. Inorg. Chem.* **1983**, *30*, 1.
(95) Hoekstra, R. M.; Telo, J. P.; Wu, Q.; Stephenson, R. M.; Nelson, S. F.; Zink, J. I. *J. Am. Chem. Soc.* **2010**, *132*, 8825.
(96) Webb, R. J.; Dong, T.-Y.; Pierpont, C. G.; Boone, S. R.; Chadha, R. K.; Hendrickson, D. N. *J. Am. Chem. Soc.* **1991**, *113*, 4806.
(97) Dong, T. Y.; Lin, M. C.; Lee, L.; Cheng, C. H.; Peng, S. M.; Lee, G. H. *J. Organomet. Chem.* **2003**, *679*, 181.
(98) Dong, T. Y.; Huang, B. R.; Peng, S. M.; Lee, G. H.; Chiang, M. Y. *J. Organomet. Chem.* **2002**, *659*, 125.
(99) Dong, T. Y.; Po, P. H.; Lai, X. Q.; Lin, Z. W.; Lin, K. J. *Organometallics* **2000**, *19*, 1096.
(100) Paul, F.; da Costa, G.; Bondon, A.; Gauthier, N.; Sinbandhit, S.; Toupet, L.; Costuas, K.; Halet, J.-F.; Lapinte, C. *Organometallics* **2007**, *26*, 874.
(101) Sutton, J. E.; Sutton, P. M.; Taube, H. *Inorg. Chem.* **1979**, *18*, 1017.
(102) Sutton, J. E.; Taube, H. *Inorg. Chem.* **1981**, *20*, 3125.
(103) Taube, H. *Ann. N.Y. Acad. Sci.* **1978**, *313*, 481.
(104) Bruce, M. I.; Low, P. J.; Costuas, K.; Halet, J.-F.; Best, S. P.; Heath, G. A. *J. Am. Chem. Soc.* **2000**, *122*, 1949.
(105) Scott, A. P.; Radom, L. *J. Phys. Chem.* **1996**, *100*, 16502.
(106) Roder, J. C.; Meyer, F.; Hyla-Kryspin, I.; Winter, R. F.; Kaifer, E. *Chem.—Eur. J.* **2003**, *9*, 2636.
(107) (a) Pelter, A.; Jones, D. E. *J. Chem. Soc., Perkin Trans. 1* **2000**, 2289. (b) Lydon, D. P.; Porres, L.; Beeby, A.; Marder, T. B.; Low, P. J. *New J. Chem.* **2005**, *29*, 972.
(108) Connelly, N. G.; Geiger, W. E. *Chem. Rev.* **1996**, *96*, 877.
(109) Krejčík, M.; Daněk, M.; Hartl, F. *J. Electroanal. Chem.* **1991**, *317*, 179.
(110) Sheldrick, G. M. *Acta Crystallogr., Sect. A* **2008**, *64*, 112.
(111) Frisch, M. J.; et al. ; *Gaussian 03*, Revision C.02; Gaussian, Inc.: Wallingford CT, 2004.
(112) Becke, A. D. *J. Chem. Phys.* **1993**, *98*, 5648.
(113) Lee, C.; Yang, W.; Parr, R. G. *Phys. Rev. B* **1988**, *37*, 785.
(114) Petersson, G. A.; Al-Laham, M. A. *J. Chem. Phys.* **1991**, *94*, 6081.
(115) Petersson, G. A.; Bennett, A.; Tensfeldt, T. G.; Al-Laham, M. A.; Shirley, W. A.; Mantzaris, J. *J. Chem. Phys.* **1988**, *89*, 2193.
(116) (a) O'Boyle, N. M.; Tenderholt, A. L.; Langner, K. M. *J. Comput. Chem.* **2008**, *29*, 839.(b) Dennington, R. D., II; Kieth, T. A.; Millam, J. M. Gaussian Inc.: Wallingford, CT, 2008.
(117) (a) Barone, V.; Cossi, M. *J. Phys. Chem. A* **1998**, *102*, 1995. (b) Cossi, M.; Rega, N.; Scalmani, G.; Barone, V. *J. Comput. Chem.* **2003**, *24*, 669.